POLITECNICO DI TORINO

Master of science in Materials Engineering for Industry 4.0

Thesis title : Design of fracture toughness specimens for additive manufacturing

Politecnico di Torino

Supervisor: Prof. Paolo Matteis

Candidate: Mohamed Walid Mohamed Mohamed Hasan

A.Y. 2025/2026

Graduation session: July 2026

Politecnico di Torino

Contents

Chapter 1: Introduction

1.1) Background: Metal Additive Manufacturing (AM) & Costs

Additive manufacturing (AM), is known as technologies that are able to build 3D physical objects from the digital 3D Computer-Aided Design models (CAD). [1]

The fundamental idea of AM is that parts are built up by the successive addition of material, in the form of 2D cross-sections, rather than by the machining away of extraneous material using, for example, the subtractive process of CNC machining, in which the part is cut from a larger solid block. In the AM process, the 3D computer aided design (CAD) model of the solid is divided into a series of serially occurring 2D cross-sections of a set minimum thickness. The AM machine can then interpret this information, and add these cross-sections together, in successively layer in a layer by layer sequence to produce the physical part: [1]

One of the key benefits of AM is the enabled "What You See Is What You Build" (WYSIWYB) feature. Since the objects are built layer-upon-layer, the level of difficulty in manufacturing does not increase with the complexity of the geometry (ease of building complex geometry). AM streamlines the entire manufacturing process by removing the bottleneck caused by preparing tooling and process planning or conducting several builds with intermediate steps to achieve complex features such as undercuts, draft angles, or internal enclosures. [1]

AM technologies can be categorized in several different ways:

1) Powder bed fusion: Processes that employ a vessel of powder fused selectively by an energy source, usually a scanning laser or an electron beam.
2) Material extrusion: processes in which a material is deposited by extruding it through a nozzle (e.g. While moving the nozzle in a set pattern to produce a part cross-section).
3) Material jetting: processes that operate in a similar way to ink-jet printing, i.e. they deposit individual droplets of the material they are built of.
4) Binder jetting: Processes where a liquid binder is jetted onto a powder bed for binding the powder particles to form the cross sections of the part.
5) Sheet lamination: processes that deposit material one layer at a time where the starting form of raw material is sheet.
6) Directed energy deposition, which involves a deposition process (most often in the form of a powder or wire feed) and an energy source, which is used to process and melt the depositing material.

1.2) Problem Statement: Cost of Standard Fracture Toughness Testing

1.2.1) The Economic Constraints of Standard Fracture Toughness Testing in Additive Manufacturing

Typically, the estimation of Mode I plane strain fracture toughness for AM materials, KIC, depends on standard test methodologies such as those in ASTM E399. With conventional subtractive manufacturing technology, such as machining a large, wrought billet, the manufacture of these large CT standards is relatively cheap and simple. All AM processes (e.g., SLM, EBM) are capable of building parts from the bottom up, layer-by-layer. As such, the build time scales with the volume and cross section of the part. So, Printing a standard, large CT specimen would take several days, making it prohibitively expensive. [1], [2], [3]

Indeed, another materials issue in AM is the cost of feedstock. Not only are post-processing heat treatments and other machine steps costly, but the raw metallic powders themselves particularly highly refined, spherical powders such as Ti alloys or specialty stainless steels are expensive to produce.[1]

1.2.2) Development of a Low-Volume, Additively Manufactured Specimen

In order to overcome the cost constraints of producing conventional CT specimen geometries, it is suggested that the creation of a low volume specimen design for AM be investigated as part of the present study. The underlying concept of this methodology draws on the freedom of form afforded by AM processing. Typically, AM is unconstrained by the tool-path considerations of standard subtractive machining, affording the ability to produce entirely unique topologies.[1],[4]

For the proposed design approach, the fundamental objective is to involve as little material as possible, that is, to reduce the total maximum profile and the unnecessary volume of the test specimen while strictly applying the essential parameters that influence the phenomenon. This means that the minimum specifications needed to sustain the plane-strain state at crack tip, i.e., specimen thickness, B, and initial uncracked ligament, W, are no different from those of the plain specimen. The material that does not directly influence the stress field at the crack tip can therefore be eliminated.[1],[2],[3]

The low-volume compact design results in a significant decrease in the time required, as well as a decrease in the powder consumed. Therefore, this approach reduces the cost of AM fracture testing and increases the number of specimens, which can be fabricated within the same build envelope, providing a larger data set of statistically significant results at no extra cost.[1]

1.2.3) the Role of the Finite Element Method (FEM) in Specimen Calibration
Though the suggested low-volume specimen geometry remedies the economic constraints of AM printing, it introduces a new analytical problem. The analytical equations and geometric calibration coefficients of international testing standards (e.g. ASTM E399) are strictly calibrated to the geometric ratios of the standard CT specimen. Since the suggested specimen does not have the standard external dimensions, the analytical equations cannot reliably be used to determine the fracture toughness. As such, numerical solutions using the FEM (in a commercial package such as ANSYS) evolve as an essential component for overcoming this analytical limitation. The numerical implementation is directed toward two main goals.[4],[5],[6]

1) Derivation of Calibration Functions (Elastic Analysis)
The first goal of the numerical investigation is to define the basic relationship between the magnitude of the applied macroscopic load, the crack length, a, and the stress field at the crack tip. For this purpose, the geometry of the suggested specimen is modeled in simple Linear Elastic Fracture Mechanics (LEFM). By performing finite element analysis for several crack to specimen width ratios (a/W), the aim is to determine the corresponding Mode I stress intensity factor, KI, for a specific magnitude of the applied force, F. Once a series of finite element predictions can be assembled for a range of crack lengths, then a new tailor-made and specialized calibration function (or geometric shape factor) can be analytically formulated which future experimental scientists working in industry can employ to determine the critical fracture toughness, KIC, while testing the new low-volume specimen within laboratory settings.

2) Numerical Validation of Fracture Equivalence (Elastic-Plastic Analysis)

Obtaining a calibration equation does not justify the specimen; a more stringent demonstration is required to convince the scientific community that this new low-volume geometry provides the same results as standard specimens. The stresses at the crack tip must be shown to be unaffected by the specimen's external boundaries. A sophisticated elastic-plastic numerical model must be employed to demonstrate this.

The validation protocol focuses on two critical fracture mechanics criteria:

1) The plastic zone is the area of localized yield that forms in front of the crack tip under load. The FEM analysis is used to derive and compare the extent of the plastic zone for the normal CT specimen as well as the new low-volume specimen. For the new design to be valid under the same applied SIF value and material, the size of the plastic zones must not be significantly greater than in the standard specimen.
2) The normal stress distribution along the un-cracked ligament between the two specimens which will be performed to assess their mechanical equivalence.

1.3) Thesis Objectives: Low-Volume Specimen Design

Primary Objective

The main objective of this work is to design, and validate a new low-volume specimen geometry specifically tailored to characterize the Mode I plane-strain fracture toughness, K_{IC}, of AM metallic alloys. This streamlined, low-volume specimen geometry strives to reduce the cost in material and in time that printing traditional fracture mechanics specimens requires.

Specific Objectives

To systematically achieve this primary goal, the research is divided into the following specific objectives:

Geometrical Design for Additive Manufacturing: To develop a reduced volume fracture specimen, which can reduce the build volume and the machine time by about 50% compared to established geometries (e.g. Standard Compact Tension specimen). This geometry will, as a first step, be constrained to maintain the essential specimen dimensions (Thickness, B, and un-cracked ligament width W) necessary to uphold plane-strain at the crack tip.

Derivation of Calibration Functions using Linear Elastic Analysis: In order to derive custom geometry calibration functions (shape factors) for the new low-volume specimen geometry. This shall be achieved by using elastic material which will define the exact mathematical relation between the applied macroscopic load, the crack length (a), and the Mode I stress intensity factor (KI).

Numerical Validation of Fracture Equivalence (by using FEM): To numerically validate the physical and mechanical validity of the low-volume specimen design proposed compared to conventional geometries using advanced FEM numerical modeling techniques. The validation process is aimed at:

Plastic Zone Analysis: Quantification and comparison of the size and shape characteristics of the crack-tip plastic zone of the novel and standard specimens.

Confirmation of the K-Dominated Zone: Investigating the local crack-tip stress fields to verify the co-existence and accurate conformity of the domain dominated by the stress intensity factor K.

Economic and Practical Feasibility: To measure the theoretical savings to raw material (metal powder) usage and machine run-time, thus to put forward the proposed geometry as the economically alternative in AM research.

1.4) Thesis Outline

In order to systematically accomplish the research purposes that have been defined in the previous sections, the present thesis is divided into six main chapters. This arrangement aims to progressively cover the work to be done starting from the theoretical aspects, through the morphological design, up to the numerical validation and the conclusions. The present work is structured as follows:

Chapter 2: Theoretical Formulation of Mode I Fracture, This chapter lays the theoretical foundations for the research and discusses the underlying principles of LEFM and EPFM. It provides an overall review of the status of the metal AM process in terms of its economic and logistical limitations of adapting the standardized macroscopic methods of fracture testing methods such as ASTM E399 to AM components. It also provides a review of the previous use of numerical modeling to obtain geometric calibration factors.

Chapter 3: Finite Element Modeling and ANSYS Implementation, This chapter describes the initial concepts and geometric reasoning pertaining to the proposed low-volume specimen. It describes design constraints that are established in order to keep geometric variables that are key to ensuring a valid plane-strain condition at the crack tip (namely B and W) constant and independent of specimen size. The chapter then sets a methodology for reducing all non-essential volume in order to reduce AM machine time and powder usage.

Chapter 4: Standard CT Specimen Geometry and Size Requirements, This chapter presents a 3D finite element model of a standard Compact Tension (CT) specimen in ANSYS, adhering to ASTM E1820 standards to establish a numerical baseline. Using a linear isotropic elastic material model, the setup features a highly refined tetrahedral mesh at the crack tip to accurately capture stress singularities. The simulation applies opposing 30,000 N bearing loads and remote displacement constraints to mimic physical testing, enabling the extraction of the Mode I Stress Intensity Factor (K_I) using the Domain Integral Method. Finally, parametric studies evaluate fracture behavior across eleven distinct crack lengths.

Chapter 5: Elastic Fracture Model Analysis for the new specimen, This chapter introduces a low-volume specimen tailored for Additive Manufacturing to reduce material use and print time compared to standard Compact Tension geometries. Evaluated in ANSYS, the finite element model uses localized Sphere of Influence (SOI) meshing at the crack tip to accurately extract the Mode I Stress Intensity Factor (KI). The analysis applies representative bearing loads and parameterizes eleven crack lengths to validate the new geometry against strict ASTM standards.

Chapter 6: Results of elastic model for standard specimen and new specimen, This chapter presents the linear elastic finite element analysis results for the standard specimens and new specimen. The Mode I Stress Intensity Factor (K_I) was calculated using the domain integral method across six concentric contours. To ensure numerical accuracy and overcome the crack-tip singularity, the innermost contour was systematically discarded, and the stabilized results from contours two through six were averaged.

Chapter 7: Plastic Fracture Model for the Standard Specimen, This chapter presents a non-linear elastic-plastic finite element analysis comparing the plastic zones of standard and sub-sized Compact Tension specimens.

Utilizing a Bilinear Isotropic Hardening model and the von Mises yield criterion, the study evaluates yielding containment under identical Mode I loading. To bypass the prohibitive computational costs of full 3D simulations, highly refined 2D half-symmetry models were utilized. Plane Strain condition was simulated at a fixed $\frac{a}{W} = 0.5$ to rigorously validate the new geometry's mechanical constraint at its physical extremes.

Chapter 8: Plastic Fracture Model for the New Specimen, This chapter outlines the setup for a non-linear elastic-plastic finite element analysis of the new specimen. Using a plastic material, the model employs a half-symmetry 2D planar approach to significantly reduce computational load while maintaining accuracy. The analysis evaluates Plane Strain condition at a fixed $\frac{a}{W} = 0.5$. A highly refined radial mesh is generated at the crack tip to capture steep stress gradients and the plastic zone. Finally, analytically derived boundary loads are applied to ensure mechanically equivalent driving forces between the models.

Chapter 9: Results of plastic model for standard specimen and new specimen, This chapter presents a non-linear elastic-plastic finite element analysis comparing the plastic zones of standard and sub-sized specimens. Utilizing a Bilinear Isotropic Hardening model for plastic material property and the von Mises yield criterion, the study evaluates yielding containment under identical Mode I loading.

Chapter 2: Theoretical Formulation of Mode I Fracture

2.1) Introduction to Mode I Fracture: Overview and the K_I Concept

At its core, a fracture (or crack growth) occurs when external stress causes a material to progressively break down, splitting it into two distinct surfaces. We analyze fractures based on how these two surfaces move relative to one another as they separate. Depending on the direction of this movement, fractures are classified into three primary modes, though real-world cracks often involve a combination of them.[7] Figure 2.1

- **Mode I:** Opening or tensile mode.
- **Mode II:** Shearing or sliding mode.
- **Mode III:** Tearing or out-of-plane mode.

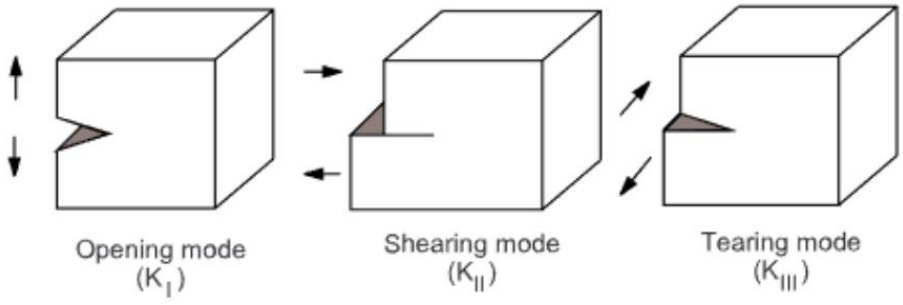

Figure 2.1: Schematic of the Fracture Modes

The Stress-Intensity Factor (K_I) quantifies the severity of the stress and deformation state in the immediate vicinity of a crack tip. Under applied loading, the stress and strain fields are most concentrated at the crack tip; K_I provides a single parameter that characterizes the magnitude of this local field.[7]

The subscript "I" just means we are dealing with a Mode I fracture this is the classic "opening" mode where forces are pulling the crack straight apart.

The characteristics of K_I:

The Infinity Problem (The Singularity): For the elastic material, pure math dictates that as you get infinitely close to the sharp tip of a crack, the stress shoots up to infinity. Since we cannot measure infinity, K_I acts as a practical way to measure the magnitude or the "size" of that intense stress.

The stress intensity factor, K_I, quantifies the magnitude of the stress field driving crack propagation under a given loading condition. Each material possesses an intrinsic, material-specific threshold known as the fracture toughness, K_{Ic}, which represents the critical value of stress intensity that the material can withstand before the onset of unstable crack growth. When the applied stress intensity factor K_I attains or exceeds this critical value K_{Ic}, the crack propagates in an unstable manner, precipitating fracture.

The Energy Connection: It takes physical energy to break the bonds inside a material and grow a crack. K_I is directly tied to the "energy-release rate" (G), which is the amount of energy available to fuel that growth. They are linked by the formula $G = \frac{K_I^2}{E^*}$ (where E^* just represents the stiffness of the material).

How Modern Software Calculates It: In the past, Dense meshes had to be used at the crack tip to try and guess the stress as it approached zero distance it was a difficult process. Today, software like ANSYS uses the Interaction Integral method. Instead of zooming in on the exact tip, it looks at the energy in a wider zone around the crack. This method is highly accurate and does not require a perfect, detailed mesh.

2.2) Need for Numerical Solutions in Fracture Analysis

Pioneers like Westergaard and Williams managed to create such equations for simple cracks using pure math. However, real-world parts are usually too complicated for these neat equations. Since we can't solve these messy, real-world shapes by hand, we rely on computer estimations to do the heavy lifting. Today, the top method for this is the Finite Element Method (FEM). Instead of struggling with tough math, FEM takes a complex object and divides it into thousands of tiny, simple blocks. A computer can easily calculate each block one by one, providing a highly accurate map of the stress around a crack.[7]

2.3) Mathematical Formulation: The Domain Integral Method

In computational fracture mechanics, determining the Stress-Intensity Factor (K) is essential for predicting crack growth, fatigue life, and failure. When analyzing cracked components with Finite Element Analysis (FEA) software like Ansys, researchers need to extract these fracture parameters from the numerical results. Modern commercial solvers mainly use Energy Methods. To understand this, one needs to consider the mathematical nature of a crack tip and the limitations of the Finite Element Method. ANSYS solves the main unknowns, which are the displacements at the nodes, but it calculates the fracture mechanics integrals, such as the J-integral or Interaction Integral, at the integration points, known as Gauss points, within the elements.[7],[8]

The Superiority of Energy Methods (Domain Integral)

To avoid the numerical instability of the crack tip, modern FEA software like Ansys uses Energy Methods, specifically the Domain Integral Method based on the J-integral. Instead of examining stresses or displacements at a single, error-prone point, the Domain Integral Method calculates the total strain energy release rate by integrating over a defined volume, or domain, of elements around the crack tip.

This approach offers several important advantages:

1. By evaluating a domain of elements that extends outward from the crack tip, the calculation relies on data far from the singularity, where the finite element shape functions are very accurate.

2. Integration is a mathematical smoothing process. By summing the energy across thousands of integration points within a volume, localized numerical errors at individual nodes are averaged out.

2.3.1) The J-integral Concept

the energy domain integral method provides a general framework for the numerical analysis of the J integral. Additionally, the domain integral formulation is fairly easy to implement numerically and is quite efficient. This method closely resembles the virtual crack extension method.

2.3.2) Domain Integral Representation of J-integral

The J integral is generally regarded as the basic variable in fracture mechanics and can be used to characterize materials using linear elastic and nonlinear elastic plastic properties. A mathematical expression can be derived for the J integral Eq.(2.1). [7]

$$J = \lim_{\Gamma \to 0} \int_{\Gamma_o} \left[w\delta_{1i} - \sigma_{ij} \frac{\partial u_j}{\partial x_1} \right] n_i \, d\Gamma$$

Eq. (2.1)

Where W is the strain energy density, σ represents the stresses, u is the displacement vector, and Γ is the contour over which the integration occurs.

For a crack in a linear elastic material, J-integral is the energy-release rate. The amplitudes of the crack-tip stress and deformation fields are also described by J-integral.

The same equation above is actually the generalized Mathematical formulation of J-integral. It is actually used to calculate the energy released per every unit area of crack extensions in any specific material, and therefore it is a significant value to estimate if the crack is more likely to grow in a linear elastic or nonlinear elastic-plastic state.

- $\lim_{\Gamma \to 0} \int_{\Gamma 0} [\dots] \, d\Gamma$: This represents the mathematical operation of integrating So, the values inside the brackets along a specific path. The limit ($\lim_{\Gamma \to 0}$) indicates that this specific general definition requires the contour to be small, meaning it hugs the crack tip infinitely closely.
- **w (or W)**: The **strain energy density**. This is the potential energy stored within the material due to deformation (stretching, compressing, or bending) as the crack is loaded.

- δ_{1i} :This is the Kronecker delta, a mathematical switch. It ensures we are only looking at the energy acting in the direction of crack extension.
- **σ_{ij}:** This represents the **stresses** acting on the material around the crack tip.
- $\frac{\partial ui}{\partial ji}$: This represents how the **displacement vector (u_j)** changes as you move along the direction of the crack (x_1 or x_1).
- **n_i**: The outward normal vector. It simply points perpendicular to the contour line Γ at any given spot, ensuring the forces are calculated in the correct direction relative to the path.

Physically, this formula balances two things happening at the crack tip:

1. The energy stored in the material as it stretches (w + T).
2. The mechanical work being done by the internal stresses (σ_{ij}) moving the material $\frac{\partial ui}{\partial ji}$.

Eq. (2.2) is written in a form that is not amenable to direct numerical computation, as there is no way to determine stresses and strains on a vanishingly small contour. If we join the inner and outer contours, shown in figure 2.2, we obtain a closed loop: the outer contour, 1, is finite and the inner one, 0, is vanishingly small.

For quasistatic conditions, the closed contour, $\Gamma^* = \Gamma_1 + \Gamma_+ + \Gamma_- - \Gamma_0$ Eq. (2.2)

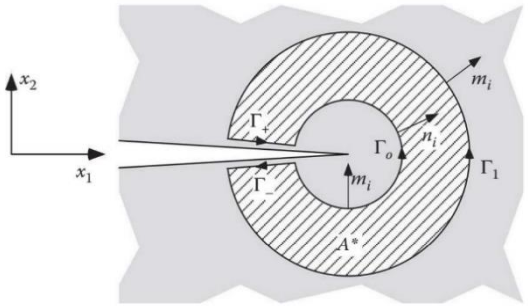

Figure 2.2 Inner and outer contours, which form a closed contour around the crack tip when connected by Γ+ , Γ-

This simple formula is a mathematical way used in computational fracture mechanics to enable computer software such as ANSYS to evaluate a crack. Computers are unable to evaluate a set of values down an "infinitely narrow" path at the crack tip.

Γ*: This represents the total, newly created closed contour (or loop) over which the calculation is performed.
Γ_1: The "outer contour." This is a finite, larger path drawn around the crack that the computer software can easily evaluate.
Γ_+: The path segment running along the (upper face) of the crack.
Γ-: The path segment running along the (lower face) of the crack.
$-\Gamma_0$: The vanishingly small "inner contour" located exactly at the sharp crack tip. (The negative sign simply means we are tracing this path in the reverse direction to close the loop).

Equation 2.1 can be written in terms of the following integral.

$$J = \int_{\Gamma^*} \left[\sigma_{ij} \frac{\partial u_j}{\partial x_1} - w\delta_{1i} \right] q m_i d\Gamma - \int_{\Gamma_+ + \Gamma_-} \sigma_{2j} \frac{\partial u_j}{\partial x_1} q d\Gamma \qquad \text{Eq. (2.3)}$$

where Γ+, Γ- are the upper and lower crack faces, respectively, m_i is the outward normal on Γ*, and q is an arbitrary but smooth function that is equal to unity on Γ_0 and zero on Γ_1. Note that $m_i = -n_i$ on Γ_0; also, $m_1 = 0$ and $m_2 = \pm 1$ on Γ_+ and Γ-

For the moment, the crack faces are traction free. So, the second term is zero. Applying the divergence theorem to Equation 2.3 gives

$$J = \int_{A^*} \frac{\partial}{\partial x_i} \left\{ \left[\sigma_{ij} \frac{\partial u_j}{\partial x_1} - w\boldsymbol{\delta}_{1i} \right] q \right\} dA \qquad \text{Eq. (2.4)}$$

$$= \int_{A^*} \left[\sigma_{ij} \frac{\partial u_j}{\partial x_1} - w\delta_{1i} \right] \frac{\partial q}{\partial x_i} dA + \int_{A^*} \left[\frac{\partial}{\partial x_i} \left(\sigma_{ij} \frac{\partial u_j}{\partial x_1} \right) - \frac{\partial w}{\partial x_1} \right] q dA \quad \text{Eq. (2.5)}$$

Where A^* is the area enclosed by Γ^*. The equation will become:

$$\frac{\partial}{\partial x_i} \left(\sigma_{ij} \frac{\partial u_j}{\partial x_1} \right) - \frac{\partial w}{\partial x_1} = 0 \quad \text{Eq. (2.6)}$$

σ_{ij}: The stress tensor.
u_j: The displacement vector.
x_1: The coordinate direction of crack growth.
ω: The strain energy density, or stress work.

The divergence of the mechanical work (the first term) is exactly cancelled by the second term, the gradient of the strain energy density in the direction of the crack axis. This is the mathematical '"engine" which maintains the path-independence of the J-integral in elastic materials:

It is convenient at this point to divide ω into elastic and plastic components

$$w = w^e + w^p = \int_0^{\varepsilon_{kl}^e} \sigma_{ij} d\varepsilon_{ij}^e + \int_0^{\varepsilon_{kl}^p} S_{ij} d\varepsilon_{ij}^p \quad \text{Eq. (2.7)}$$

By splitting, the total stress work into two parts: Elastic Component So, Stored energy that can be recovered. In addition, Plastic Component in which Energy dissipated through permanent material deformation.

In continuum mechanics, it is crucial to distinguish between the total stress, denoted as **σ_{ij}** , and the deviatoric stress tensor, denoted as S_{ij}. The total stress **σ_{ij}** encompasses all internal forces acting on a material element, including both the hydrostatic stress component—which governs elastic volumetric changes and the shear components. In contrast, the deviatoric stress S_{ij} isolates the shape distorting forces by subtracting the mean hydrostatic stress from the total stress tensor ($S_{ij} = \sigma_{ij} - \sigma_m \delta_{ij}$).

Taking account of the plastic strain, thermal strain, body forces, and crack face tractions leads to the following general expression for J in two dimensions:

$$J = \int_{A^*} \left\{ \left[\sigma_{ij} \frac{\partial u_j}{\partial x_1} - w\delta_{1i} \right] \frac{\partial q}{\partial x_i} + \left[\sigma_{ij} \frac{\partial \varepsilon_{ij}^p}{\partial x_1} - \frac{\partial w^p}{\partial x_1} + \alpha \sigma_{ii} \frac{\partial \Theta}{\partial x_1} - F_i \frac{\partial u_j}{\partial x_1} \right] q \right\} dA - \int_{\Gamma_+ + \Gamma_-} \sigma_{2j} \frac{\partial u_j}{\partial x_1} q d\Gamma \quad \text{Eq. (2.8)}$$

Equation 2.8 is reduced to equation 2.9 by eliminating body forces, thermal strains, and crack face tractions.

$$J = \int_{A^*} \left[\sigma_{ij} \frac{\partial u_j}{\partial x_1} - w\delta_{1i} \right] \frac{\partial q}{\partial x_i} dA$$

Eq. (2.9)

2.4 Interaction Integral Method: Actual and Auxiliary Crack-Tip Stress Fields

The Interaction Integral (I-Integral) for Mode Decoupling

To resolve the inability of the J-integral to separate mixed-mode fracture parameters, the Interaction Integral (I-integral) method is utilized. This technique isolates the individual Stress-Intensity Factors (SIFs)—K_I, K_{II}, and K_{III}—by introducing analytical auxiliary fields.[7]

The domain representation of the Interaction Integral (I_0) evaluated at a specific point on the crack front is given by:

Auxiliary Fields (aux): These denote highly controlled, analytically derived asymptotic crack-tip fields (stresses σ^{aux}, strains ε^{aux}, and displacements u^{aux}) corresponding to pure Mode I, pure Mode II, or pure Mode III loading.

$$I_0 = -\frac{\int_V q_{,j} \left[\sigma_{kl} \varepsilon^{aux}_{kl} \delta_{ij} - \sigma^{aux}_{kj} u_{k,i} - \sigma_{kj} u^{aux}_{k,i} \right] dV}{\int_S \delta q_n \, dS}$$

Eq. (2.10)

$q_{i,j}$: The spatial derivative of the weight function.

The denominator serves to normalize the volume integral, localizing the extracted parameter to a specific nodal location on the crack surface S.

The Interaction Integral and the Domain J-Integral are fundamentally linked through the principle of superposition. Because the strain energy density (ω) inherent to the J-integral is a quadratic function of stress and strain, the J-integral itself is non-linear.

If two independent equilibrium states are superimposed—State 1 being the actual FEA boundary value problem (σ^1_{ij}, ε^1_{ij}, u^1_i) and State 2 being the analytical auxiliary field (σ^2_{ij}, ε^2_{ij}, u^2_i)—the total J-integral of the superimposed state expands as follows:

$$J_{total} = J^{(1)} + J^{(2)} + I^{(1,2)}$$

Eq. (2.11)

The term $I^{(1,2)}$ is the Interaction Integral, which arises as the cross-term from the expansion of the strain energy density.

$$J_{total} = \frac{(K^{(1)}_I + K^{(2)}_I)^2}{E^*} + \frac{(K^{(1)}_{II} + K^{(2)}_{II})^2}{E^*} + \frac{(K^{(1)}_{III} + K^{(2)}_{III})^2}{2\mu}$$

Eq. (2.12)

$$I^{(1,2)} = \frac{2}{E^*} (K^{(1)}_I K^{(2)}_I + K^{(1)}_{II} K^{(2)}_{II}) + \frac{1}{\mu} (K^{(1)}_{III} K^{(2)}_{III})$$

Eq. (2.13)

- As the more concering to the **Mode I:** Opening or tensile mode.

  According to the relationship between the energy release rate (J) and the stress-intensity factors (K) in Linear Elastic Fracture Mechanics (LEFM), the total J-integral can also be expressed in terms of the superimposed SIFs:

$$J_{total} = \frac{(K_I^{(1)} + K_I^{(2)})^2}{E^*} \quad \text{Eq. (2.14)}$$

  By expanding this quadratic expression and equating it to the superimposed J_{total} equation, the terms representing the pure actual state ($J_{(1)}$) and the pure auxiliary state ($J_{(2)}$) cancel out.
  The remaining mutual energy terms explicitly define the Interaction Integral ($I_{(1,2)}$):

$$I^{(1,2)} = \frac{2}{E^*}(K_I^{(1)} K_I^{(2)} \quad \text{Eq. (2.15)}$$

  During each iteration, the software strategically alters the theoretical "auxiliary field" to isolate a specific fracture mode:

1. **(Isolating Mode I - K_I):** The software defines the auxiliary field as a pure Mode I state. It assigns a unit value to the Mode I auxiliary SIF ($K_I(2)=1$) and sets the other auxiliary components to zero (KII(2)=0, KIII(2)=0).

   Consequently, the generalized interaction integral equation mathematically reduces to: $I_1 = \frac{2}{E^*} k_I^1$ This allows the actual Mode I stress-intensity factor ($K_{I(1)}$) to be explicitly extracted.

   Therefore, The biggest benefit of using the Interaction Integral approach instead of the conventional J-integral approach is that this method is capable of mathematically separating mixed-mode fracture components. Instead of outputting a summed total strain energy where the modal components were not individually known, the software is able to employ three mutually exclusive auxiliary fields to allow it to perform three separate integrations.

Chapter 3: Finite Element Modeling

Finite element mesh construction involves both craftsmanship and artistry. Even with the aid of pre-processing and post-processing software, a human must still input knowledge and judgment in order to create the best model possible (not to mention handle crack problems). The following section addresses these core issues of crack related meshing. When analyzing a real-world structure, cracks are rarely perfectly flat or two-dimensional. Instead, a 3D crack propagates along a continuous front (the crack front). Evaluating fracture parameters across such a front requires transitioning from a 2D line integral to a 3D volume integral.[5]

In a two-dimensional domain, the crack tip is a singular point, and the J-integral is evaluated along a 2D closed curve surrounding it. In a three-dimensional domain, the crack tip is extended into a line or a curve known as the crack front. The fracture mechanics parameters (such as the J-integral or Stress Intensity Factors, K_i) fluctuate locally at each node along this front due to changing through-thickness constraint effects. Therefore, evaluating the energy release rate requires isolating individual point-like segments along the 3D crack front.[7]

3.1) isolating a finite segment

The theoretical generalization of the J-integral from two-dimensional planar configurations to three-dimensional continuous bodies represents a critical advancement in computational fracture mechanics. By establishing a local orthogonal coordinate system along a continuous crack front, the methodology transitions from highly sensitive surface integrations to more numerically stable volume integrations through the application of the divergence theorem. This domain integral formulation utilizes a localized weighting function, q, which acts as a normalized, non-uniform virtual crack advance to isolate the strain energy calculations to specific finite element nodes. Ultimately, this discrete algorithmic approach provides the robust mathematical foundation required for modern finite element solvers to accurately extract pointwise fracture parameters, reliably accounting for the continuous variations in energy release rates across complex three-dimensional geometries.[7]

As illustrated in **Figure 3.1** , analyzing a 3D crack necessitates isolating a finite segment, denoted by length ΔL, along the continuous crack front, η. To evaluate the local fracture parameters at any given point on this front, a local orthogonal coordinate system is established. In this framework, x_1 is normal to the crack front, x_2 is perpendicular to the crack plane, and x_3 is tangent to the crack front.

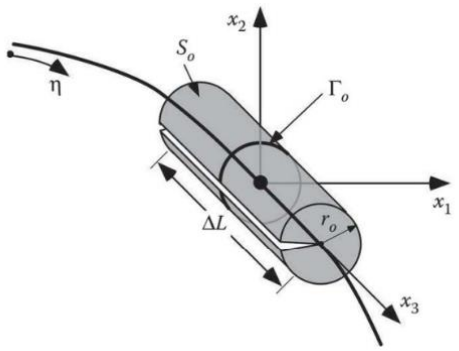

Figure 3.1: Surface enclosing an increment of a 3D crack front

Rather than relying on a simple 2D contour (Γ_o), the 3D formulation constructs a theoretical tube with a small radius r_o and an outer surface area S_o around the specified segment ΔL. Under typical quasistatic loading conditions, the local value of the J-integral, $J(\eta)$, does not remain constant but varies continuously along the length of the crack front, where η represents a specific coordinate position along a continuous crack front, while $J(\eta)$ denotes the localized, pointwise value of the J-integral evaluated at that exact location.[7]

To account for this variation, Eq. (3.1) introduces a weighting function, q, to compute a weighted average of the energy domain, $\bar{J}$, over the increment ΔL. The full expression demonstrates that this weighted average is obtained by evaluating the limit as the tube's radius r_o goes to zero. The corresponding surface integral over S_o incorporates the stress work (w) and the spatial derivatives of the displacement field (u_j) relative to the local coordinate system. Ultimately, this formulation provides the robust mathematical foundation required to extract accurate fracture parameters from 3D finite element models.

$$\bar{J}\,\Delta L = \int_{\Delta L} J(\eta) q\, d\eta = \lim_{r_o \to 0} \int_{S_o} \left[w\delta_{1i} - \sigma_{ij} \frac{\partial u_j}{\partial x_1} \right] q n_i\, dS \qquad \text{Eq. (3.1)}$$

Figure 3.2 illustrates the physical interpretation of the mathematical weighting function, q, within the context of a three-dimensional virtual crack extension analysis. While q fundamentally serves as a smooth mathematical device to construct a domain integral, assigning it a physical analog helps clarify how local fracture parameters are extracted numerically along a continuous, curved crack front.[7]

In a three-dimensional domain integral formulation, the energy release rate typically varies continuously along the crack front. To isolate and evaluate the local value of the J-integral mathematically, the function q is defined as a normalized, non-uniform virtual displacement applied across a finite crack front segment of length ΔL.

The mechanics depicted in the schematic can be broken down as follows:

- **Localized Virtual Extension:** Rather than advancing the entire, continuous crack front uniformly, a localized, bell-shaped virtual extension is simulated exclusively over the increment ΔL. Beyond this segment, q vanishes to zero, preventing boundary contributions from the end surfaces of the localized control volume.
- **The Weighting Function (q):** At any given point along ΔL, the local virtual crack advance, $\Delta a(\eta)$, is expressed as a function of its position via the relation $\Delta a(\eta) = \mathbf{q}\,(\eta)\,.\,\Delta a_{max}$. q scales between 0 at the boundaries of the segment and 1 at the location of maximum virtual advance.
- **Incremental Area Generation:** The shaded region represents the total incremental crack area, ΔA_c, generated by this localized virtual extension. Mathematically, this area is the integral of the local extension across the segment, expressed as:

$$\Delta A_c = \Delta a_{\max} \int_{\Delta L} q(\eta)\, d\eta \qquad \text{Eq. (3.2)}$$

By mapping the mathematical function q to a virtual, physical displacement field, finite element codes can apply virtual shifts to nodal coordinates within localized domains. This localized weighting provides the essential framework for extracting highly accurate, pointwise distributions of the J-integral along complex, curved three-dimensional crack fronts.[7]

Figure 3.2 illustrates the geometric construction of a closed control surface, S^*, used to define the weighted average J-integral over a segment of a three-dimensional crack front. This formulation is essential for transitioning from a surface integral to an energy domain volume integral (V^*), rendering the problem highly amenable to numerical evaluation in finite element analysis.[7]

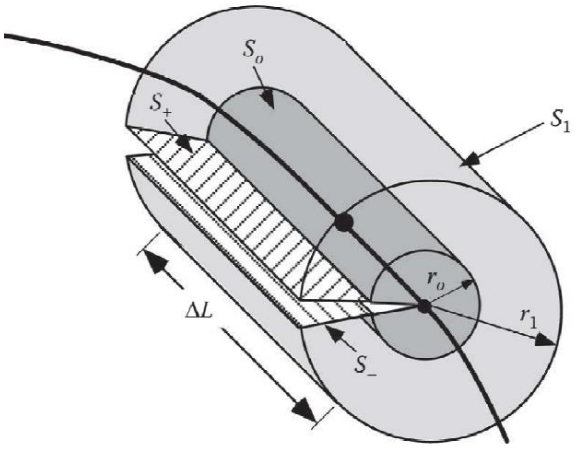

Figure 3.2: inner and outer surfaces, S_o and S_1, which enclose V^*

The specific architectural components of this 3D control volume include:

- **The Crack Front Segment (ΔL):** The primary curved axis representing the local segment of the crack front under evaluation.
- **Inner Surface (S_o):** An internal cylindrical tube of radius r_o directly bounding a finite segment of the crack tip front.
- **Outer Surface (S_1):** A second, larger concentric tube of radius r_1 constructed around the crack front to establish a finite domain for integration.
- **Crack Faces (S_+ and S_-):** The upper (S_+) and lower (S_-) planar surfaces of the crack flanking the crack plane that are physically enclosed between the radii r_o and r_1.
- **Enclosed Volume (V^*):** The annular solid domain bounded internally by S_o, externally by S_1, and along the flanks by the crack faces S_+ and S_- over the segment length ΔL.

This geometric configuration acts as the three-dimensional analogue to the 2D closed contour integration path. By establishing this closed **surface** boundary mathematically defined as, $S^* = S_1 + S_+ + S_- - S_o$ the divergence theorem can be effectively applied. This mathematical transformation enables codes to convert a highly sensitive surface integral into a far more stable volume integration over the localized domain V^*.[7]

To ensure the validity of this localized volume evaluation, the weighting function q must be defined such that it smoothly transitions to zero at both longitudinal ends of the segment $\Delta\mathbf{L}$, effectively isolating the calculation from any non-physical boundary contributions from the end caps of the cylinders.

The next section outlines the mathematical transition required to calculate the J-integral for a three-dimensional crack using finite element analysis (FEA). Specifically, it demonstrates how to convert a complex surface integral into the **Domain Integral formulation**.

Equation 3.3 starts by defining the average J-integral over a crack segment (ΔL) as an integral over a closed 3D surface (S^*).

$$\overline{J}\,\Delta L = \int_{S^*}\left[\sigma_{ij}\frac{\partial u_j}{\partial x_1} - w\delta_{1i}\right]qm_i dS - \int_{S_+ + S_-}\sigma_{2j}\frac{\partial u_j}{\partial x_1}qdS \qquad \text{Eq. (3.3)}$$

However, calculating stresses and strains along a specific surface in a computer model is highly sensitive to mesh design and prone to numerical error.

Equation 3.4 is the breakthrough. Using a mathematical rule called the divergence theorem, the surface integral is converted into a **volume integral** (V^*). This equation is comprehensive; it calculates the energy available for crack growth while accounting for complex real-world factors like plastic deformation (ε_{ij}^{P}), thermal expansion (Θ), and body forces (F_i) as a general case.[7]

As mentioned, the function q acts as a mathematical "virtual push" along the crack front. The Equation **3.4** specifies a critical boundary condition: q must equal **0** at both ends of the segment $\Delta\mathbf{L}$. If q did not drop to zero at the edges, the artificial end-caps of the cylindrical volume would improperly add extra energy to the J-integral calculation, skewing the results.

$$\overline{J}\,\Delta L = \int_{V^*}\left\{\left[\sigma_{ij}\frac{\partial u_j}{\partial x_1} - w\delta_{1i}\right]\frac{\partial q}{\partial x_i} + \left[\sigma_{ij}\frac{\partial \varepsilon_{ij^p}}{\partial x_1} - \frac{\partial w^p}{\partial x_1} + \alpha\sigma_{ii}\frac{\partial \Theta}{\partial x_1} - F_i\frac{\partial u_j}{\partial x_1}\right]q\right\}dV - \int_{S_+ + S_-}\sigma_{2j}\frac{\partial u_j}{\partial x_1}qd\Gamma \qquad \text{Eq. (3.4)}$$

Equation 3.4 calculates an average energy over the whole segment ΔL, to extract J-integral value at a specific, location on the crack front $J(\eta)$, Equation 3.5 is used, by dividing the volume-averaged result by the integral of the q function.

$$J(\eta) \approx \frac{\bar{J}\,\Delta L}{\int_{\Delta L} q(\eta, r_o)\, d\eta} \qquad \text{Eq. (3.5)}$$

3.2) Finite element implementation

To calculate the energy release rate in an FEA model, the analyst must first define the specific area (in 2D models) or volume (in 3D models) where the mathematical integration will take place.

For Inner and Outer Boundaries, this integration region is bounded by an inner contour, Γ_o, which is typically assigned directly to the crack tip. The outer boundary of this region, Γ_1, must align cleanly with the edges of the finite elements within the computer model. In 2D problems, the integration domain is a flat area. In 3D problems, establishing this domain is more complex because it becomes a volume, and the J-integral, J(η), usually needs to be evaluated at multiple discrete locations along the continuous crack front. Once the geometric domain is established, the FEA software requires a mathematical rule to dictate how the "virtual crack advance" is distributed across the nodes of the mesh. This is handled by the weighting function q. [5],[7]

- **Strict Boundary Rules:** The function q must be explicitly defined at every single node located within the integration area or volume. The fundamental requirement is that q = 1 at the inner contour (the crack tip) and q = 0 at the far outer boundary.
- **Arbitrary Internal Shape:** As long as those strict boundary conditions are satisfied, the exact shape of how q transitions from 1 down to 0 across the interior elements is mathematically arbitrary.

Figure 3.3, 3.4 visually demonstrates two common mathematical approaches for shaping this q function across a simple 2D grid of elements:

1) The Pyramid Function (Figure 3.3): The value of q is exactly 1 at the specific crack tip node and then decreases linearly to 0 in all directions. In computational fracture mechanics, the Pyramid Function often referred as a tent function or a linear hat function which is a highly localized spatial distribution used to evaluate the J-integral via the domain integral method. When implementing this numerically, the scalar function $q(x_i)$ is mathematically mapped as a localized virtual nodal displacement field at the crack tip. [7]

The shape of the pyramid function is governed by strict boundary conditions across the defined integration area (A^*):

At the Crack Tip Core, q = 1. The peak of the pyramid sits precisely on the node corresponding to the crack tip position. At the Outer Boundary (Γ1), q = 0. The base of the pyramid drops cleanly to zero where the integration domain ends. Across the Interior Elements, the function decays linearly from 1 to 0 in all directions (x1 and x2). For any intermediate node l within the mesh, its specific scalar weighting factor ql is determined by its fractional distance between the tip and the outer boundary.

Within any given quadrilateral element in the domain, the continuous distribution of q is interpolated from these discrete nodal values using the element's standard shape functions (N_i):

$$q(x_i) = \sum_{l=1}^{n} N_l q_l$$

Eq. (3.6)

n (Lowercase) is total number of Nodes, This variable denotes the total number of discrete nodes constituting a single finite element. For instance, if the model employs a two-dimensional quadrilateral element, n = 4. Conversely, when utilizing a three-dimensional element—such as a hexahedral (brick) element in a Compact Tension (CT) specimen model—n assumes a value of 8 for linear (first-order) elements, or 20 for higher-order (quadratic) elements.

N_I (Uppercase) is shape function, Also referred to as interpolation functions, these are fundamental to the finite element method. Analytically, simulation solvers (e.g., ANSYS) compute exact primary variables (such as displacements or the scalar weighting function, q) exclusively at the discrete nodal coordinates. To evaluate these variables at any continuous point within the element's interior domain, the software employs the shape functions, N_I. These functions operate as relative spatial weights, defining the proportional influence of each discrete node on the specific internal point being calculated.

As shown in **Figure 3.3**, the pyramid function represents a non-uniform virtual crack advance, when the FEA solver executes the discretized domain integral formula, it evaluates the spatial derivatives of the q function ($\frac{\partial q}{\partial x_i}$) at each integration (Gauss) point. Because the pyramid function slopes continuously downward from the peak to the base, its spatial gradient is non-zero everywhere within the integration domain.

This means that every single element covered by the pyramid's slope actively contributes to the calculated energy release rate. The stiffness variations and stress/strain fields of the elements immediately adjacent to the crack tip are heavily weighted because the slope ($\frac{\partial q}{\partial x_i}$) close to the peak is steep.

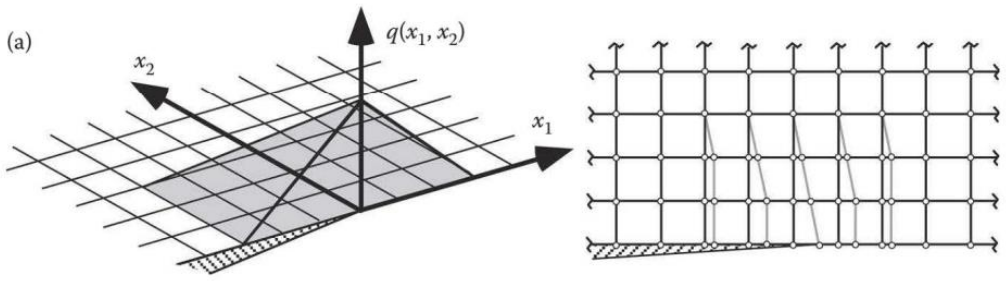

Figure 3.3: Pyramid Function (q function)

2) The Plateau Function (Figure 3.4): The value of q remains completely flat at 1 across multiple elements near the crack tip, only sloping down to 0 at the outermost ring of boundary elements.[7]

the Plateau Function represents a specific spatial distribution strategy for the weighting function, $q(x_i)$. While it satisfies the identical fundamental boundary conditions as the Pyramid Function, its internal geometry is strategically designed to isolate and eliminate the mathematical influence of the elements immediately surrounding the crack tip.

The spatial distribution of the plateau function is characterized by a broad, flat inner region that only decays at the outer edges of the domain.

- **The Crack Tip:** The function begins at q = 1 at the crack tip (the inner contour, Γ_o).
- **The "Plateau":** Unlike the pyramid function, which immediately slopes downward, the plateau function remains completely flat at q = 1 across multiple concentric rings of elements extending outward from the crack tip.
- **The Outer Ring:** The function only transitions and decays linearly from 1 down to 0 within the single outermost ring of elements making up the defined integration domain ($\Gamma 1$).

The primary mechanical calculation of the domain integral evaluates the stress work and strain fields multiplied by the spatial gradient of the weighting function, $(\frac{\partial q}{\partial x_i})$, Because the plateau region is perfectly flat, its spatial derivative in this zone is mathematically zero ($(\frac{\partial q}{\partial x_i}) = 0$). Consequently, when the finite element solver integrates the energy equations over the entire domain, the mathematical terms for any element located directly under this flat plateau are multiplied by zero. The plateau function is highly beneficial for improving the stability and accuracy of complex simulations, particularly in elastic-plastic or large-strain problems. [5], [6]

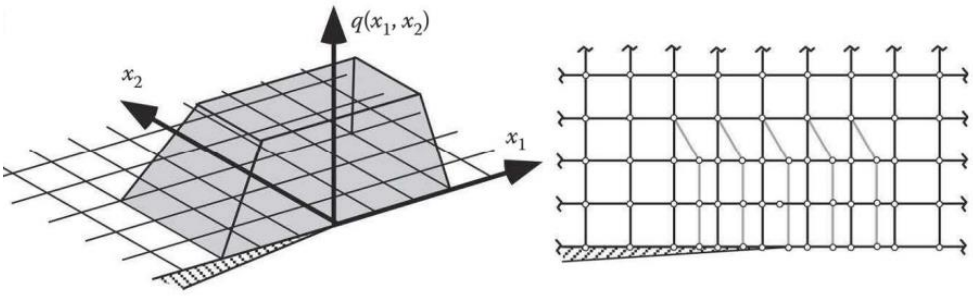

Figure 3.4: Plateau Function (q function)

3.3) Crack Definition and Local Coordinate Systems

Since the stress gradients are very high near the crack tip, the finite element modeling of a component with a crack must focus on this region.

Since the stress and displacement fields have high gradients close to the crack tip, which greatly depend on the material properties and the part geometry, a very fine local mesh must be used.

Generating a 3D fracture model is a non-trivial exercise. Ansys Mechanical has some user-friendly tools to generate structured hexahedral mesh of semi-elliptic cracks. Ansys meshes the essential crack tip region using tetrahedral elements, whenever the aperture shape is random or irregular.

Additionally, Ansys provides a wide array of user controls to fine-tune the mesh in these localized areas.

The transition from the defined hexahedral mesh at the crack front to the far field is smooth and continuous Figure 3.5. The Ansys model was used to generate a near-field tetrahedral mesh of the crack for the Ansys Mechanical model[4]. An example of this mesh around the arbitrary crack in an X-joint is shown in the following:

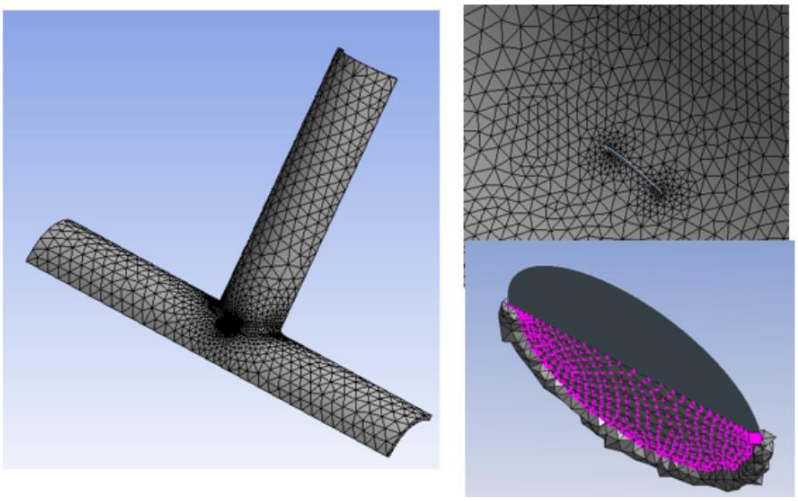

Figure 3.5: Tetrahedral Mesh for an Arbitrary Crack [4]

To obtain reliable stress-intensity factors, a local coordinate system at the crack tip must be very well defined by the local asymptotic crack tip coordinate system: x-axis should have been parallel to the crack front extension, y axes should have been strictly normal to the crack face while z axis should have pointed to the tangential crack front direction.[9] Figure 3.6

The local coordinate systems must stay perfectly consistent at each node along the crack front in order for the calculations to be accurate. In Ansys , the local coordinate systems are created based on the value of input crack front.

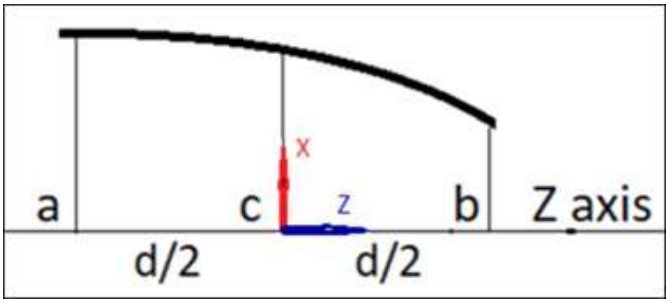

Figure 3.6: Crack-Tip Coordinate System [9]

For 3D flat crack geometries, a particular crack-tip node component has to be defined that includes all of the nodes on the crack front. Only one node should exist in each position in space. In addition, these nodes have to be connectable through their element connectivity in order to reproduce the specific line of the crack front. Ansys uses this crack front to determine exactly what elements to then use for the contour integration. The whole process is quite similar to the 2D crack geometry setup, only this time extended through all the nodes that comprise the 3D front

Chapter 4: Elastic Fracture Model for the standard specimen

The Compact Tension (CT) specimen is one of the most widely utilized standard geometries for fracture toughness testing, specifically for determining the plane-strain fracture toughness (KIC) and conducting elastic fracture mechanics (EFM) evaluations. Its design is highly favored because it requires less material volume to achieve the necessary constraint conditions compared to other standard geometries, such as the Single-Edge Notch Bending (SENB) specimen. The dimensional configurations and testing protocols for the CT specimen are strictly governed by international standards, predominantly ASTM E399 and ISO 12135.[2],[3]

4.1) standard specimen dimension

To ensure consistency and comparability of fracture toughness results, the standards dictate that all dimensions of the CT specimen must be strictly proportional to the effective width W. The effective width is defined as the distance from the load-line (the center of the pinholes) to the back edge of the specimen. Figure 4.1 represents the standard specimen used.

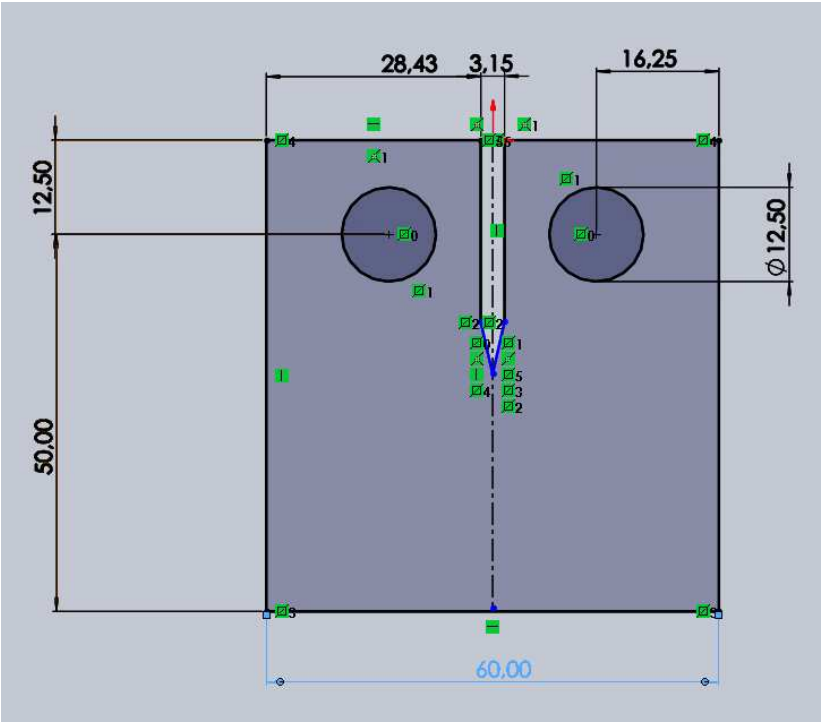

Figure 4.1: the standard specimen

In accordance with standard proportional requirements for fracture toughness testing, a reference Compact Tension CT specimen was designed with an effective width W of 50 mm.

To ensure the validity of K_{IC} evaluations, the distance from the load-line to the end of the crack (a) must fall within the standardized normalized range of $0.45 \leq a/W \leq 0.55$. Furthermore, following the conventional

dimensional configuration, a thickness-to-width ratio of B/W = 0.5 was adopted, resulting in a nominal specimen thickness B of 25 mm.

4.2) The Baseline Numerical Representation

A comprehensive three-dimensional finite element (FE) model of the standard Compact Tension (CT) specimen was developed using ANSYS Mechanical (Release 2025 R2) to serve as the baseline for geometric validation. The numerical representation was carefully established to capture the elastic behavior and the stress singularity at the crack tip.

4.2.1) Material Model: Linear Isotropic Elasticity

Prior to the design and analysis of the proposed low-volume specimen, it is necessary to establish a rigorously validated numerical baseline using the standard Compact Tension (CT) geometry. The purpose of this baseline model is to validate the finite element methodology against the well-established analytical solutions of ASTM E1820 and thereby confirm the accuracy of the modelling approach, especially in the region around the crack tip.

To serve this reference function correctly, the standard CT specimen model must use the same numerical methods and assume the same material model as the novel geometry, ensuring that any observed differences in the results are attributable solely to geometric changes and not to inconsistencies in the material model. The selected material represents an commonly steel utilized one in both traditional wrought production and advanced Additive Manufacturing (AM) processes. Within the finite element framework, the domain was mathematically defined using an linear-elastic constitutive model. The fundamental macroscopic mechanical response of the material is governed by a designated Young's modulus E of 200 GPa and a Poisson's ratio of 0.3.

4.3) coordinate systems and meshing

In Finite Element Analysis (FEA), the precise definition of local coordinate systems is critical for accurate modeling. These local systems are essential for defining highly refined, localized mesh zones (Spheres of Influence) to the crack tip and applied forces areas. Numerically, a refined mesh in these zones is required to achieve solution convergence and prevent the generation of artificial stress artifacts caused by improper load transfer between elements.

Meshing is the process of dividing a continuous geometry into a large number of small pieces called elements, which are connected to each other at points called nodes. Once this division is done, the solver can treat each small element individually using simple equations, and by assembling all these equations together, it builds a complete picture of how the entire structure behaves under load. The meshing method is set to Tetrahedrons, with a Quadratic element order. The domain discretization is strategically partitioned into distinct refinement zones: the global bulk region, the crack tip singularity zone, and the two active load-pin interfaces.

Table 4.1clearly illustrates the use of both global and local coordinate systems within Ansys. While the global coordinate triad is visible in the upper middle surface of the specimen to orient the overall workspace, the model itself features multiple specialized local coordinate systems. Figure 4.2 represents the all coordinate systems used.

Table 4.1 : Center of meshing spheres

Center of the sphere				
X (mm)	Y (mm)	Z (mm)	Radius of the sphere (mm)	Element size (mm)
0	-30	0	10	0.6
0	-30	12.5	10	0.6
0	-30	-12.5	10	0.6
-25	-12.5	6.25	10	0.7
-25	-12.5	0	10	0.7
-25	-12.5	-6.25	10	0.7
25	-12.5	6.25	10	0.7
25	-12.5	0	10	0.7
25	-12.5	-6.25	10	0.7

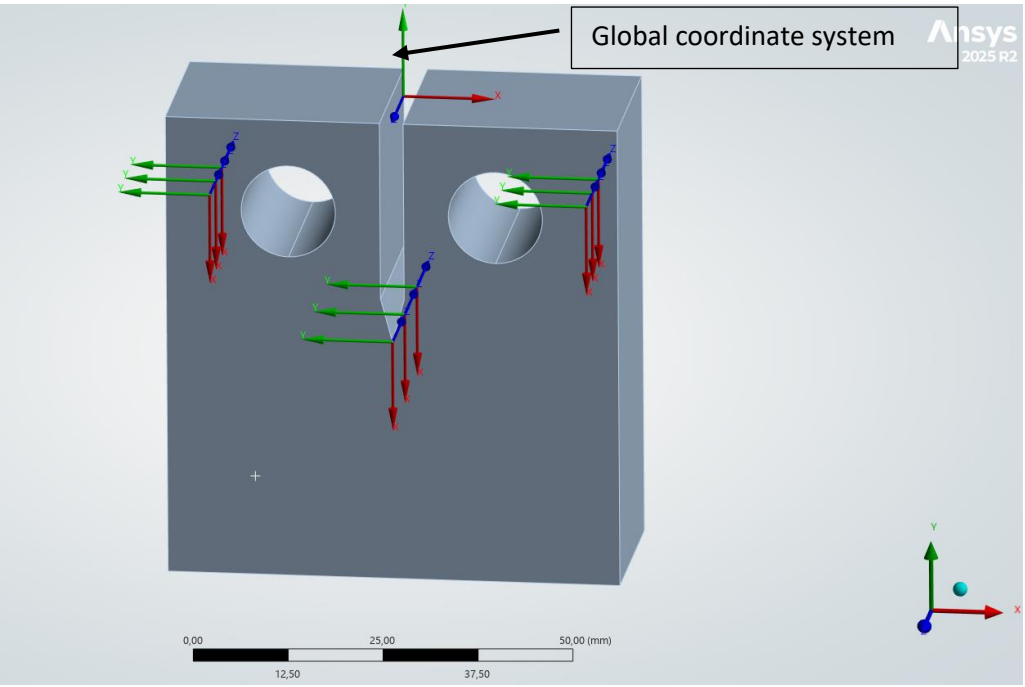

Figure 4.2: placement of coordinate systems

Figures 4.3, 4.4, 4.5 , 4.6 and 4.7 illustrate the targeted meshing strategy employed for the compact tension specimen. The resulting mesh features a highly refined, dense network of elements in these localized zones of interest, which smoothly transitions into a coarser mesh throughout the bulk of the material. This approach ensures high precision where fracture mechanics and stress concentrations are evaluated, while optimizing overall computational efficiency for the simulation.

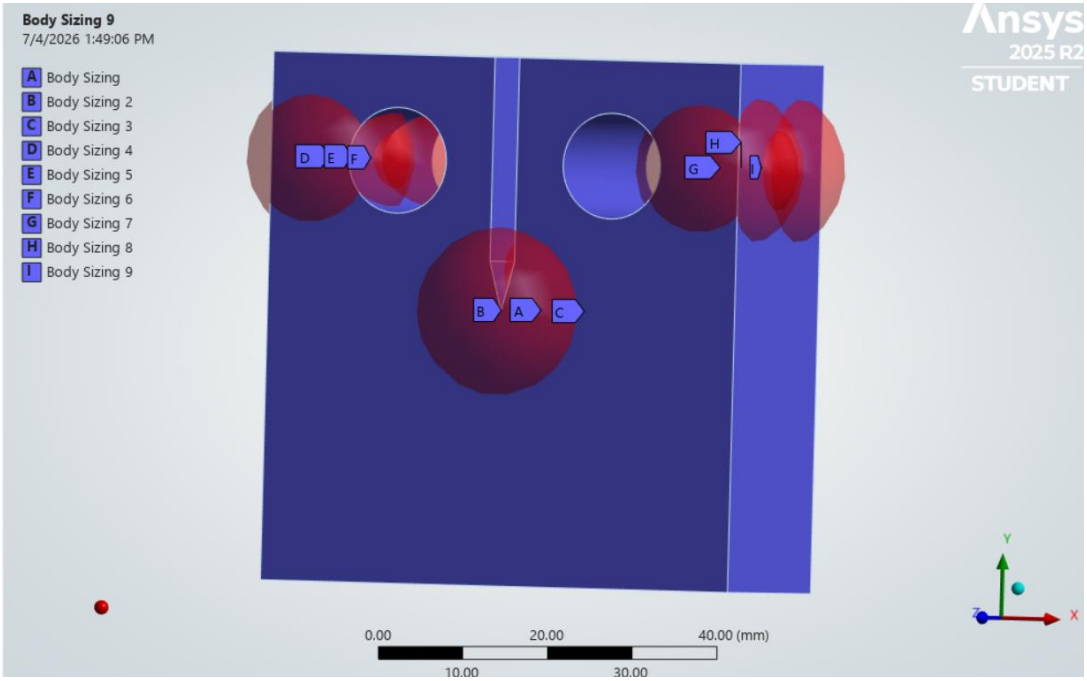

Figure 4.3: placement of meshing spheres of influence

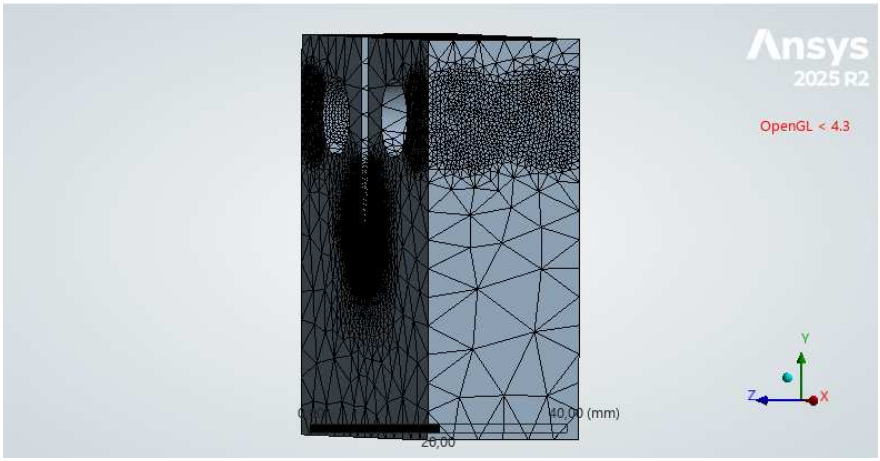

Figure 4.4: the specimen meshing

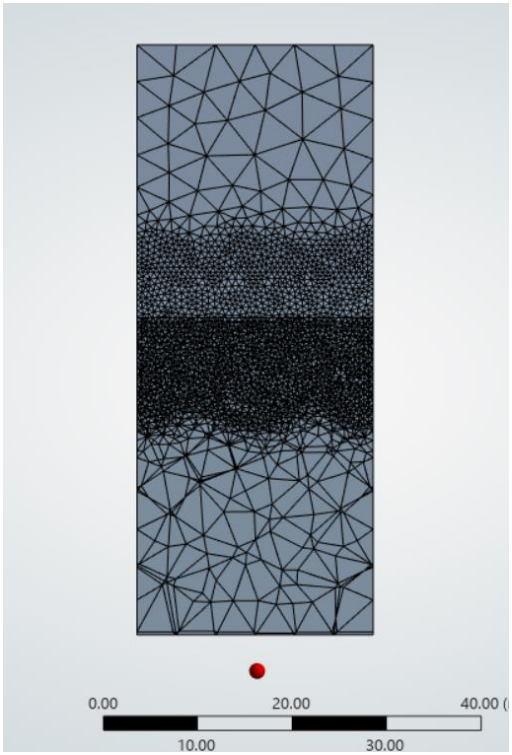

Figure 4.5: cross-section through the vertical axis

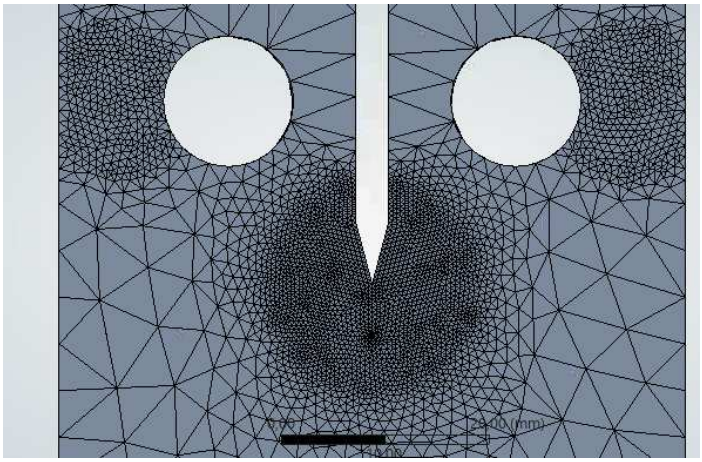

Figure 4.6: the specimen meshing

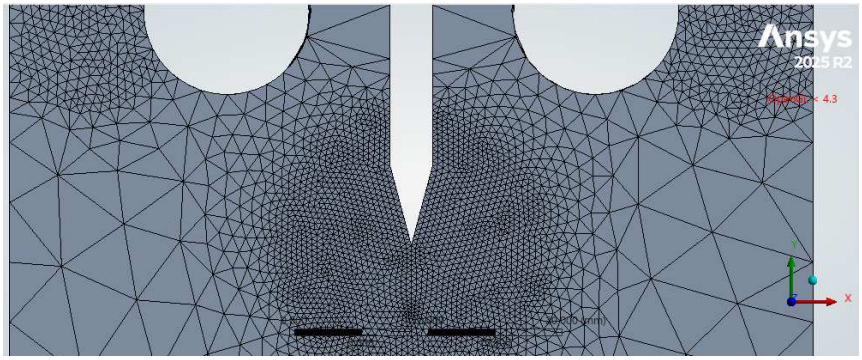

Figure 4.7: meshing of the crack tip and pin-hole

The baseline discretization initially comprised 293,937 nodes and 212,096 elements, utilizing predominantly 10-node higher-order tetrahedral elements (SOLID187). To ensure an accurate representation of the stress singularity and facilitate fracture analysis, the ANSYS SMART Crack Growth tool was subsequently integrated to optimize the local mesh topology around the crack front. This refinement process increased the mesh density to a final configuration of 699,724 nodes and 509,176 elements, thereby ensuring the resolution required for reliable extraction of fracture mechanics parameters.

4.4) Fracture Mechanics Setup

The SIF is numerically evaluated utilizing the specialized crack calculation tools within ANSYS Mechanical. The crack front and crack surfaces were explicitly defined using predefined node components, establishing a precise local coordinate system at the crack tip.

To extract the Stress Intensity Factor (KI). the J-integral is used over a volume domain surrounding the crack front and converts it into equivalent stress intensity factors. Also, To ensure numerical accuracy and confirm the path independence of the solution, the J-integral was evaluated across 6 concentric contours configured within the structured singularity mesh. The consistency of the K_I values across the outer contours serves as an indicator of a converged and mesh-independent solution.

The crack shape was specified as Edge (Crack Shape: Edge), which defines a straight-fronted, through thickness crack extending from one free surface of the specimen to the other. This crack shape is geometrically consistent with the idealized pre-crack assumed in the analytical LEFM calibration formulae of ASTM E1820 for the CT specimen, wherein the crack front is treated as a straight line parallel to the specimen thickness direction. As illustrated in Figure 4.8

The crack width was modelled uniformly at a/W = 0.45 at the start, mid, and end positions, confirming a straight, non-tapering crack front through the specimen thickness. This value matches the pre-crack configuration for the analyzed a/W ratio, with the crack applied across the full thickness. Later, by parameterization, the crack length was varied according to the a/W range specified by ASTM E1820 ($0.45 \leq a/W \leq 0.55$). Figure 4.9

Details of "Edge Crack"

Scope	
Source	Analytical Crack
Scoping Method	Geometry Selection
Geometry	1 Body
Definition	
Crack ID	119
Coordinate System	Coordinate System
Crack Shape	Edge
P --Start Width	5, mm
P --End Width	5, mm
P --Mid Width	5, mm
--Depth	25, mm
Mesh Method	Tetrahedrons
Largest Contour Radius	0,6 mm
Growth Rate	Default (1,2)
Front Element Size	0,20 mm
Mesh Contours	6
Solution Contours	Match Mesh Contours
Suppressed	No
Buffer Zone Scale Factors	
X Scale Factor	1,2
Y Scale Factor	1,2
Z Scale Factor	1,2

Figure 4.8 : edge crack setting

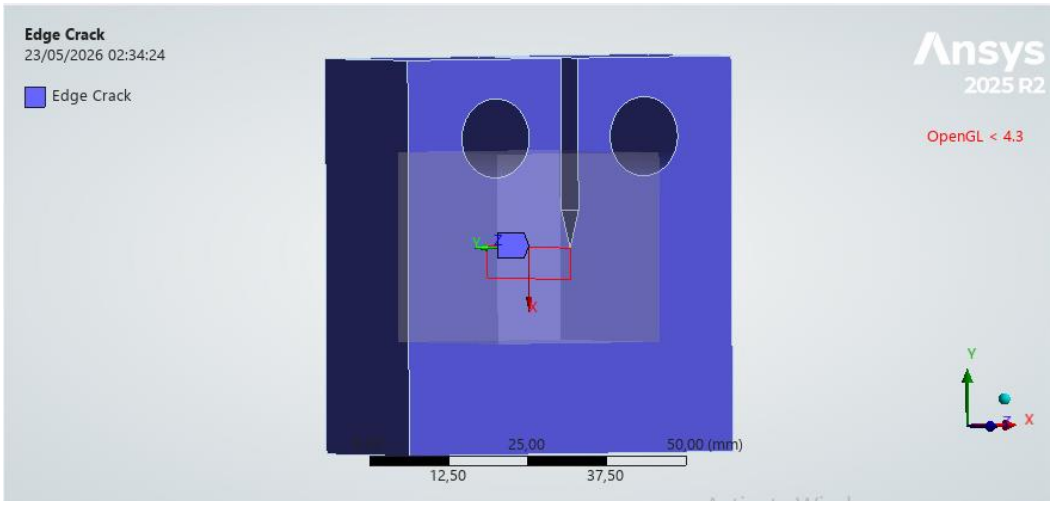

Figure 4.9 : edge crack in the specimen

The crack-front region was meshed using the Tetrahedrons mesh method (Mesh Method: Tetrahedrons), consistent with the unstructured tetrahedral mesh employed across the bulk of the CT specimen. The use of tetrahedral elements in the vicinity of an analytically defined edge crack is managed automatically by the ANSYS fracture toolset through its internal Unstructured-Mesh Method (UMM), which ensures that fracture parameters computed on tetrahedral meshes achieve the same accuracy as those obtained from structured hexahedral meshes

The radial extent of the crack-front integration domain was controlled by the Largest Contour Radius parameter, set to 0.6 mm. This value defines the outer radius of the annular region of structured elements surrounding the crack front within which the domain integral is evaluated. The contour radius must be large enough to encompass sufficient elements for path-independence of the J-integral, yet small enough to remain well within the K-dominated zone — the annular region ahead of the crack tip where the singular stress field governed by K_1 is dominant. A radius of 0.6 mm satisfies both criteria for the mesh density employed in this study

The Growth Rate was set to the Default (1,2) value, which controls the geometric progression ratio of element sizes from the crack-front node outward through successive contour rings. A growth rate of 1.2 produces a smooth, gradual increase in element size from the highly refined crack-tip zone to the coarser bulk mesh, preventing abrupt element size transitions that could introduce numerical ill-conditioning into the stiffness matrix.

The Front Element Size was specified as 0.20 mm, defining the characteristic element edge length of the innermost ring of elements directly attached to the crack-front nodes. This level of refinement ensures that the steep stress and strain gradients in the immediate vicinity of the crack tip are adequately resolved by the finite element shape functions, and that the collapsed wedge-shaped singularity elements at the crack front can accurately reproduce the $1/\sqrt{r}$ stress singularity required by LEFM.

The number of integration contours was set to 6 Mesh Contours (Mesh Contours: 6), with the Solution Contours configured to Match Mesh Contours. This instructs the solver to evaluate the domain J-integral and the interaction integral across six successive concentric rings of elements radiating outward from the crack front. In accordance with standard practice in computational fracture mechanics, the result from Contour 1 which contains the singular crack-tip elements and is therefore most susceptible to numerical error is

discarded, and the fracture parameters reported correspond to the mean of the stable values obtained from Contours 2 through 6. Path-independence across these outer contours serves as the primary criterion for the validity and convergence of the extracted stress intensity factor K_I.

The J-integral has a fundamental theoretical property, its value must be identical regardless of which path choosing to evaluate it around the crack tip.

In reality, the crack tip contains a mathematical stress singularity that stresses theoretically shoot to infinity at that exact point. This creates a critical problem for the finite element solver, So, six contours are used:

Contour 1 (closest to the crack tip): sits inside this singularity-dominated zone, where no mesh no matter how fine can accurately capture the stress field. With Contour 1, the singularity is at the centre and so the results are very sensitive to numerical errors and hence are typically discarded. The six concentric rings of elements radiating outward from the crack tip can be presented like the rings of a tree trunk. Figure 4.10

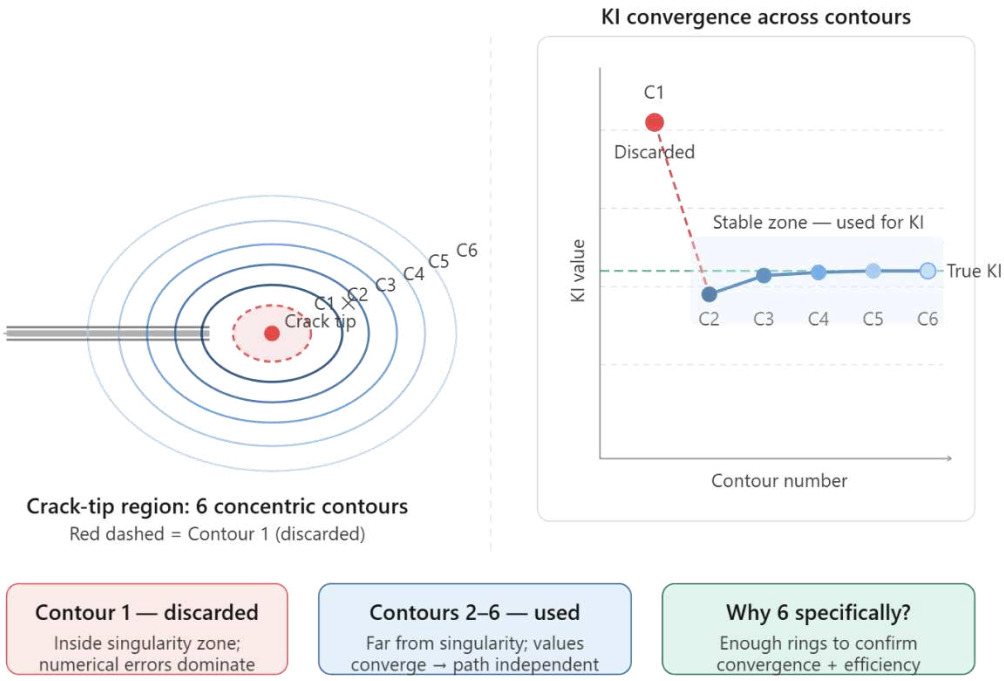

Figure 4.10: contours explanation

Using only 2 or 3 contours gives almost no margin to verify convergence. Discard Contour 1. Each additional contour ring extends further from the crack tip toward the model's outer boundaries. If a contour ring reaches the specimen's geometric edge or a loading pinhole, it "sees" the farfield loading directly and the result becomes contaminated. Contouring cannot extend beyond the outer geometric limits of the model without invalidating the results.

| Contour 1 | Always discarded — lives inside the singularity.
| Contours 2–3 | First usable results, but still relatively close to the tip.
| Contours 4–6 | Confirmation zone — if these three agree with each other, convergence is proven.

So with six contours, contour 1 is discarded, So, the other five contours are usable readings, which can clearly demonstrate that the last five are stable and converging which is exactly the mesh quality validation the examiner expects to see.

4.5) Boundary Conditions and Applied Loading

A rigorously defined set of boundary conditions and loading configurations was implemented within the finite element model of the Compact Tension (CT) specimen. The complete boundary condition scheme, as established in ANSYS Mechanical (Release 2025 R2) and depicted in Figure 4.11, and table 4.2 comprises two opposing bearing loads applied to the pinhole bores and three remote displacement constraints.

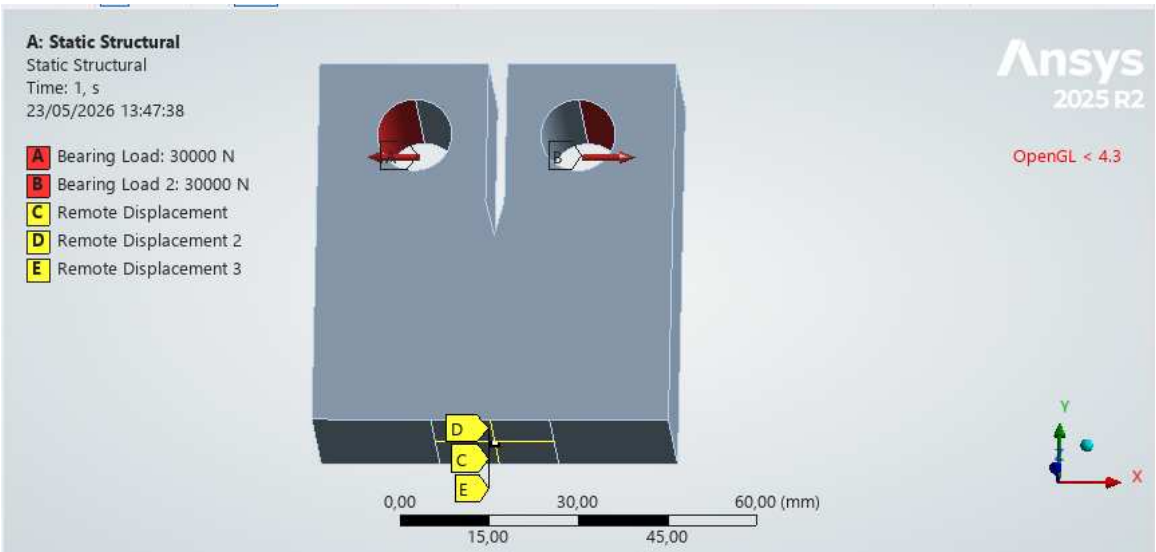

Figure 4.11: Boundary condition configuration of the standard CT specimen.

Table 4.2 Complete boundary condition configuration of the standard CT specimen FE model.

Condition	Location	Geometry	X (m)	Y (m)	Z (m)	Rot X (°)	Rot Y (°)	Rot Z (°)
Bearing Load 1	Left pinhole	1 Face	−30,000 N	0	0	—	—	—
Bearing Load 2	Right pinhole	1 Face	+30,000 N	0	0	—	—	—
Remote Disp. 1	Lower surface	Edge C	0 (fixed)	Free	Free	Free	Free	0 (fixed)
Remote Disp. 2	Lower surface	Edge D	Free	Free	0 (fixed)	0 (fixed)	Free	Free
Remote Disp. 3	Lower surface	Vertex E	Free	0 (fixed)	Free	Free	0 (fixed)	Free

The tensile driving force required to initiate and sustain Mode I crack-tip loading was introduced through two Bearing Loads applied, respectively, to the inner cylindrical face of the left pinhole (Bearing Load 1) and the inner cylindrical face of the right pinhole (Bearing Load 2). Both loads were defined in the Global Coordinate System using component-based input, with a magnitude of **30,000 N** assigned exclusively to the *X*-direction component, while the *Y*- and *Z*-direction components were set to zero. The two loads are oriented in opposing senses

The *Bearing Load* formulation was preferred over simplified point-force or uniform-pressure boundary conditions because it distributes the applied force over the projected compressive contact area of the pin bore in a cosine-shaped pressure distribution, accurately replicating the non-uniform contact stress field that arises from a rigid cylindrical pin acting against the hole surface. This physically representative loading method prevents the introduction of artificial stress concentrations inherent in idealized point-load applications, and ensures that the local deformation field at the loading holes develops in a mechanically consistent manner.

Three *Remote Displacement* constraints were defined to eliminate rigid body motion and to impose the appropriate kinematic degrees of freedom at the specimen–fixture interfaces. All three constraints were scoped using Geometry Selection and were referenced to the Global Coordinate System.

For Remote Displacement 1 (edge C of the lower surface as the model), the boundary conditions were: X = 0 m (ramped), constraining lateral sliding of the lower grip; Y = Free, allowing vertical displacement as the crack mouth opens; Z = Free, permitting out-of-plane compliance; Rotation X = Free; Rotation Y = Free, accommodating angular deflection from crack mouth opening; and Rotation Z = 0° (ramped), preventing in-plane rigid body rotation of the lower arm.

For Remote Displacement 2, (edge D of the lower surface as the model), the boundary conditions were: X = Free, Y = Free; Z = 0 m (ramped), preventing out-of-plane translation of the upper grip; Rotation X = 0° (ramped); Rotation Y = Free, permitting in-plane angular compliance; and Rotation Z = Free. This configuration constrains out-of-plane and in-plane rotational rigidity at the upper loading point while preserving the horizontal and vertical degrees of freedom required for realistic crack-mouth opening behaviour.

For Remote Displacement 3, applied at a single vertex at the lower centeral surface, the boundary conditions were: X = Free; Y = 0 mm (ramped); Z = Free; Rotation X = Free; Rotation Y = 0° (ramped); Rotation Z = Free.

The collective effect of this boundary condition scheme is to produce a statically determinate, physically representative simulation of the CT specimen under monotonic Mode I loading. The opposing bearing loads drive symmetric crack-tip opening displacement, while the three remote displacement constraints suppress rigid body motion without imposing artificial stiffness on the fracture-critical regions of the model. This configuration provides the mechanical basis for the reliable extraction of the Mode I stress intensity factor, K_1, and the J-integral from the finite element solution, as reported in the subsequent sections.

4.6) Solver Configuration:

The finite element solution was executed using **ANSYS Mechanical APDL 2025 R2** under a static structural analysis framework. The analysis was configured as a linear elastic, steady-state static solution, consistent with the assumptions of Linear Elastic Fracture Mechanics (LEFM). The key solver parameters extracted directly from the solution output are summarized as follows:

The equation solver employed was the **Distributed Sparse Matrix Direct Solver**, operating across **2 parallel MPI processes** on an Intel Xeon Gold 6252N CPU (2.30 GHz). This solver type is well-suited for large, sparse symmetric stiffness matrices generated by the predominantly tetrahedral SOLID187 mesh.

The discretized model comprised a total of 699,724 nodes and 509,176 elements, with the dominant element type being the 10-node higher-order tetrahedral SOLID187. The full system of equations solved by the sparse solver involved 2,099,195 degrees of freedom (DOF) which equals the total number of equations, reflecting the three translational and three rotational DOF per node introduced by the remote displacement constraint elements

The total solution elapsed time was approximately 8,549 seconds (~2.37 hours), with the equation factorization phase accounting for the dominant share of the computational effort. The sparse direct solver achieved a sustained computational rate of 33.5 GFlops, indicating that the allocated processor cores successfully executed 33.5 billion floating-point operations per second with an effective I/O rate of 0.9 GB/s, the relatively low I/O rate being consistent with out-of-core operation. The total disk space consumed by all solver files reached 46.9 GB, and the total I/O written and read from disk amounted to 227.6 GB and 272.2 GB respectively.

4.7) Parameterization

The calculation was repeated by changing crack length to be equal [0.45 : 0.01 : 0.55]*W and the way in which it is calculated was explained before in section (4.5) Fracture Mechanics Setup.

The average stress intensity factor is extracted automatically at each design point upon solution convergence. For each of the eleven design points, ANSYS Workbench automatically performed the following sequence without user intervention:

1. Updated the crack length parameter in the analytical crack definition
2. Regenerated the local crack-tip mesh while preserving all other mesh settings
3. Executed the full static structural solution under identical boundary conditions and loading
4. Extracted output parameter after simulation
5. Stored the results in the Table of Design Points for post-processing

Chapter 5 : Elastic Fracture Model for the new specimen

This study introduces a novel, low-volume fracture mechanics specimen. Traditional standard specimens, such as Compact Tension (CT) or Single-Edge Notch Bending (SENB), are more low-cost for machining, leading to prolonged print times, increased material consumption, and a heightened susceptibility to print-induced thermal residual stresses. By employing new design, we tried to develop a new specimen geometry that significantly reduces both mass and overall volume. Figure 5.1

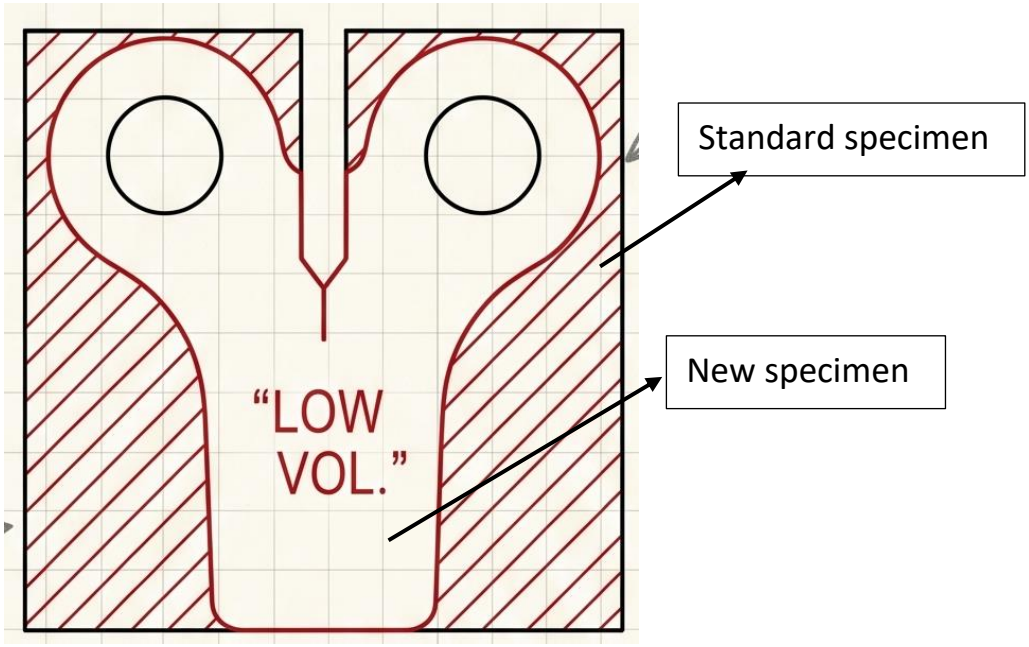

Figure 5.1: Standard specimen and new specimen

The geometric development of standardized fracture mechanics specimens has historically been driven by the need to balance mechanical testing requirements with ease of fabrication. Traditional geometries, such as the Compact Tension (CT) specimen, were inherently designed to maintain a low volume while remaining highly compatible with conventional subtractive manufacturing processes, such as milling from standard flat plates. Similarly, the disk-shaped compact specimen was optimized for straightforward machining from cylindrical bar stock. Accordingly, the low-volume geometry proposed in this study does not introduce a fundamentally novel design philosophy. Rather, it represents a continuation of this established paradigm, adapting the principles of geometric modification and design for manufacturability to the unique processing capabilities of additive manufacturing.

5.1) New Specimen Geometry and Size Requirements

This is a modified fracture mechanics specimen designed as an alternative to the standard Compact Tension (CT) specimen. The geometry features a dual-pin loading configuration with a slotted body, intended to improve plastic zone distribution through the thickness.

The standard Compact Tension (CT) specimen, as defined by ASTM E399, represents the conventional geometry employed in plane strain fracture toughness testing. Its rectangular profile and sharp fatigue pre-crack are used for generating a dominant plane strain stress state at the crack tip, facilitating valid K_{IC} measurements.

The following sections describe each geometric difference between standard specimen and the new specimen.

The most visually apparent distinction between the two geometries lies in their external boundary profiles. The standard CT specimen maintains a strictly rectangular outer envelope, with all edges meeting at 90° corners and no geometric features beyond the functional notch and pin holes. Which make it is easy to machine from bulk material, so that increase weigh without usefulness.

In contrast, the proposed specimen adopts an dual-lobe profile, wherein the upper region of the specimen transitions into two circular lobes that protrude beyond the rectangular envelope of the standard geometry. The lower body retains a quasi-rectangular form but with fully filleted corners of radius $R = 0.1W$, eliminating all re-entrant sharp corners. This modification serves to remove unloaded material.

In the standard CT specimen, the two loading pin holes of diameter $Ø = 0.25W$ are positioned symmetrically within the rectangular body at a vertical distance of $0.275W$ from the specimen centerline, with their centers lying on the load line. The surrounding material remains flat, and load is introduced directly through pin bearing against the hole walls. Figure 5.2

In both specimen, the effective width (w) is 50 mm, the thickness (B) is 25 mm and the initial crack length fall within the range of $0.45 \leq a_0/W \leq 0.55$.

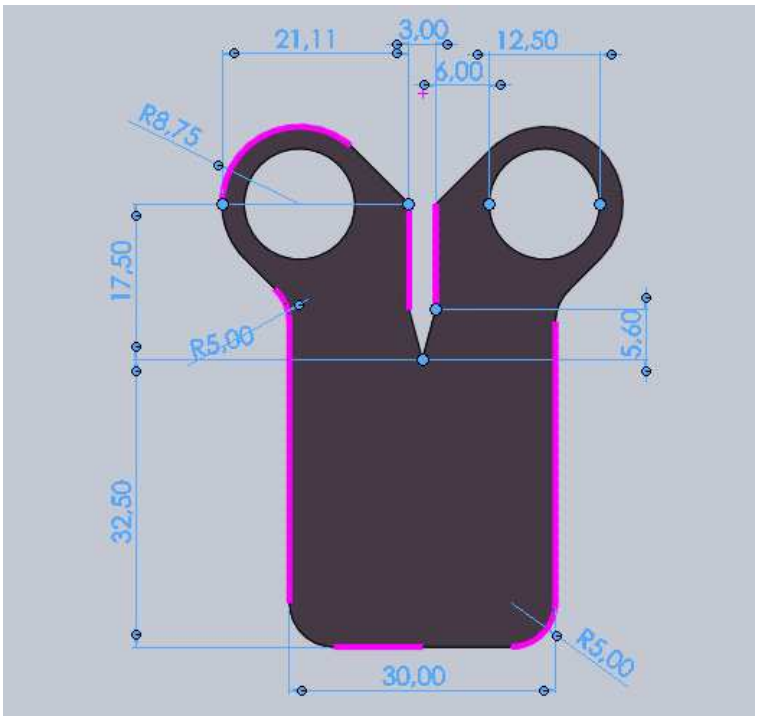

Figure 5.2: new specimen dimension

The standard specimen has a volume of 85483 mm³ and a mass of 0,666 kg, while the new specimen reduces this to 39184 mm³ and 0,307 kg. Replacing the standard geometry with the new one therefore yields a 53% reduction in material consumption.

5.2) coordinate systems and meshing

Consistent with the standard specimen model, nine local coordinate systems were defined, each associated with a corresponding mesh sphere of influence (SOF). Table 5.1 presents the coordinates of these local coordinate systems together with their respective SOF.

Figure 5.3 represents the local coordinate systems, Figure 5.4 represents the (SOFs), Figure 5.5 , 5.6, 5.7 represent the specimen after meshing

Table 5.1: coordinates of local coordinate systems together with their respective SOF

Center of the sphere				
X (mm)	Y (mm)	Z (mm)	Radius of the sphere (mm)	Element size (mm)
0	-30	12.5	10	0.6
0	-30	0	10	0.6
0	-30	25	10	0.6
21	-12.5	0	10	0.7
21	-12.5	12.5	10	0.7
21	-12.5	25	10	0.7
-21	-12.5	0	10	0.7
-21	-12.5	12.5	10	0.7
-21	-12.5	25	10	0.7

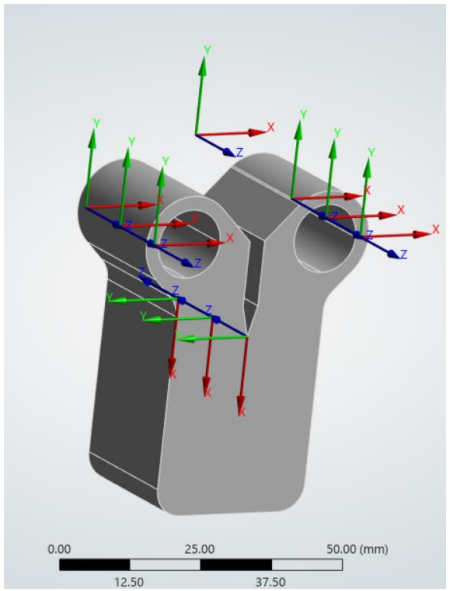

Figure 5.3 the local coordinate systems

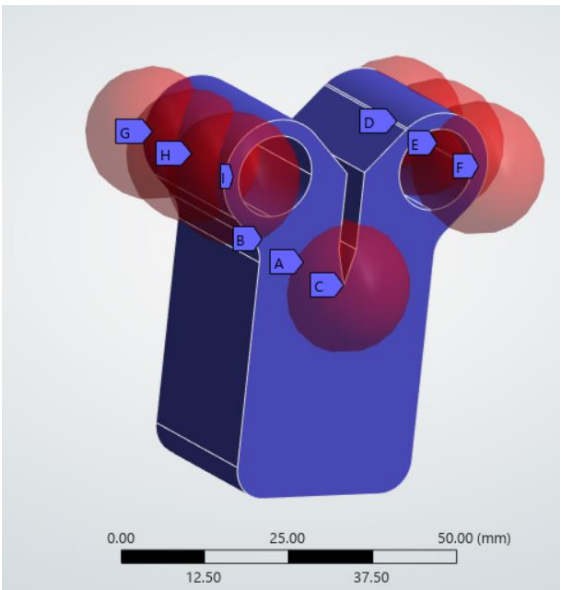

Figure 5.4: spheres of influence

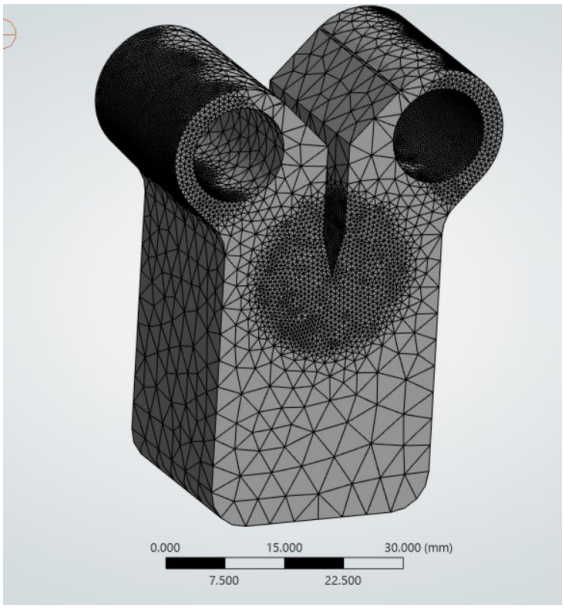

Figure 5.5: specimen meshing

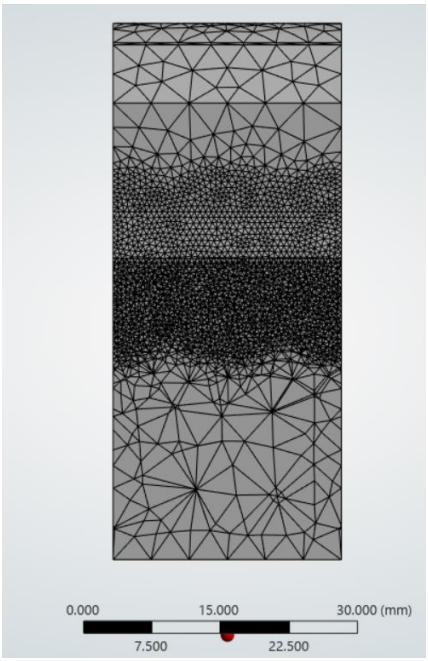

Figure 5.6: cross-section specimen meshing

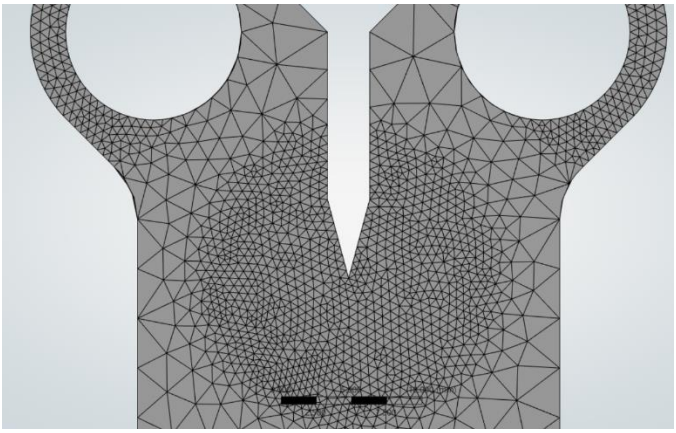

Figure 5.7: gradient of the meshing

5.3) Boundary Conditions and Applied Loading

Applied forces and constraints are the same like the standard specimen model and Figure 5.8 represent the two bearing forces and the three remote displacements applied to the specimen.

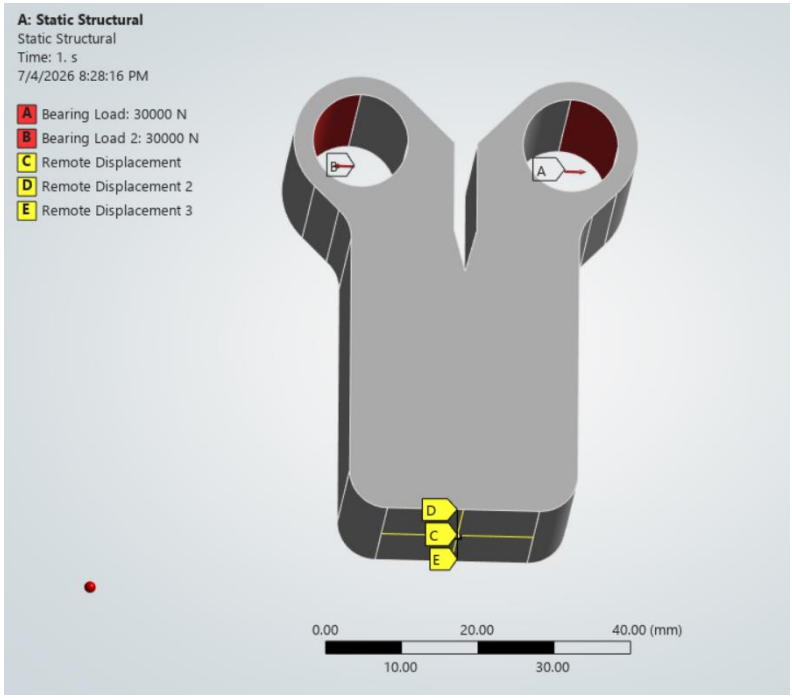

Figure 5.8: boundary condition of the new specimen

For the analysis setting, the solver configuration and Parameterization, the new specimen used the same like the standard specimen model which was mentioned in the previous chapter.

Chapter 6 : Results of elastic module for standard specimen and new specimen

6.1) Results of standard specimen

Upon the successful completion of the automated parametric study within the ANSYS framework, the Mode I Stress Intensity Factor (KI) was extracted systematically across six concentric integration contours surrounding the crack tip.

In three-dimensional cracked geometries, K_I varies through the specimen thickness due to the shift from plane-stress conditions at the free surfaces to plane-strain conditions at the mid-plane, producing a characteristic parabolic through-thickness distribution. Since analytical formulas such as those in ASTM E1820 are based on idealized two-dimensional, uniform-field assumptions, they cannot capture this local variation. Averaging K_I along the crack front is therefore necessary to obtain an equivalent macroscopic value consistent with the two dimensional analytical solution, providing a rigorous basis for validating the numerical model.

Figure 6.1 represent the SIF for the standard specimen for crack size a/w = 0.45. Contours 2 through 6 overlap almost completely due to their close numerical agreement, so only Contour 1 (which departs visibly due to its proximity to the crack-tip singularity) remains distinguishable in the plot.

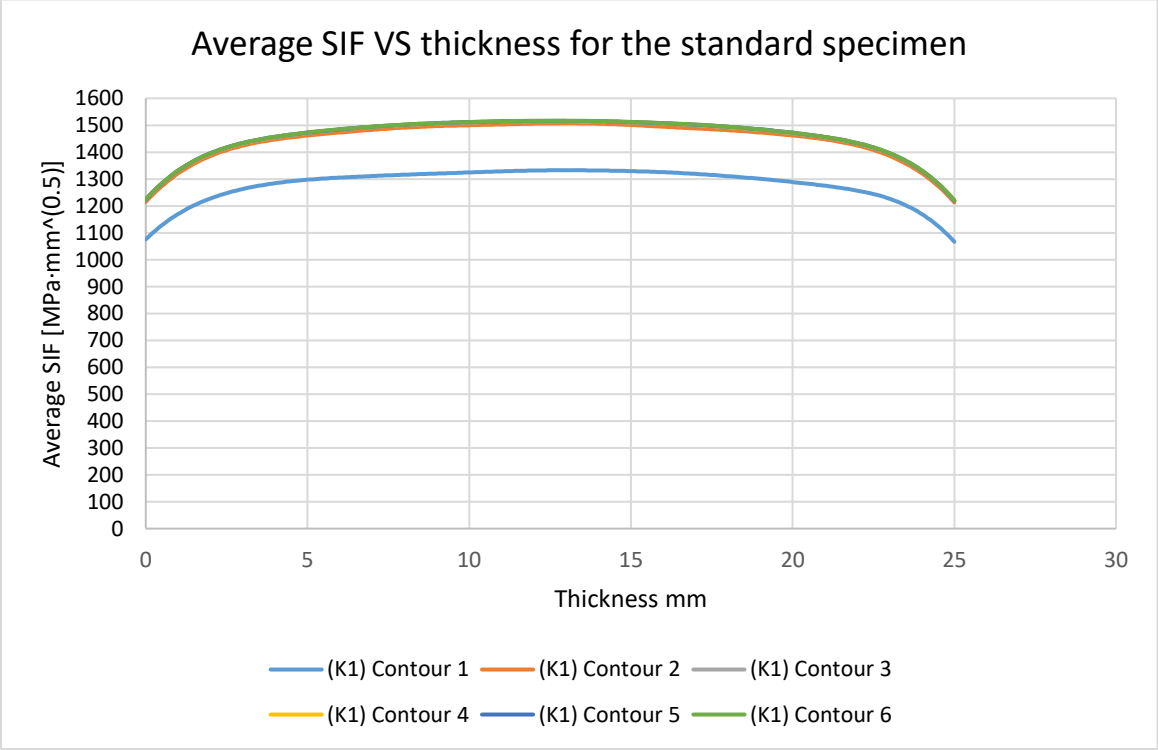

Figure 6.1: the SIF for the standard specimen for crack size a/w = 0.45

As illustrated in table 6.1, the numerical calculation of the standard CT specimen demonstrates excellent agreement with the theoretical ASTM E1820 predictions. A quantitative assessment reveals that the relative

error between the 3D numerical model and the theoretical standard remains strictly **below 3%** across the entire parametric range.

Table 6.1: Theoretical and numerical calculation of the standard CT

Crack length (mm)	a/w	Theoretical K (MPa√mm)	Average K from simulation (MPa√mm)	Difference between theoretical and simulation
5.00	0.45	1415.27	1455.97	2.83%
5.50	0.46	1455.98	1496.60	2.75%
6.00	0.47	1498.57	1539.63	2.70%
6.50	0.48	1543.19	1585.59	2.71%
7.00	0.49	1590.00	1632.98	2.67%
7.50	0.50	1639.20	1682.06	2.58%
8.00	0.51	1690.98	1734.86	2.56%
8.50	0.52	1745.56	1790.93	2.57%
9.00	0.53	1803.17	1849.58	2.54%
9.50	0.54	1864.08	1911.04	2.49%
10.00	0.55	1928.58	1976.73	2.47%

Figure 6.2 presents the evolution of the Mode I Stress Intensity Factor (K_I) as a function of the normalized crack length across the standard validity domain of $0.45 \leq a/w \leq 0.55$. The plot compares the analytical baseline derived from the ASTM E1820 empirical formulations for the standard specimen (blue curve) against the computationally extracted numerical results (orange curve).

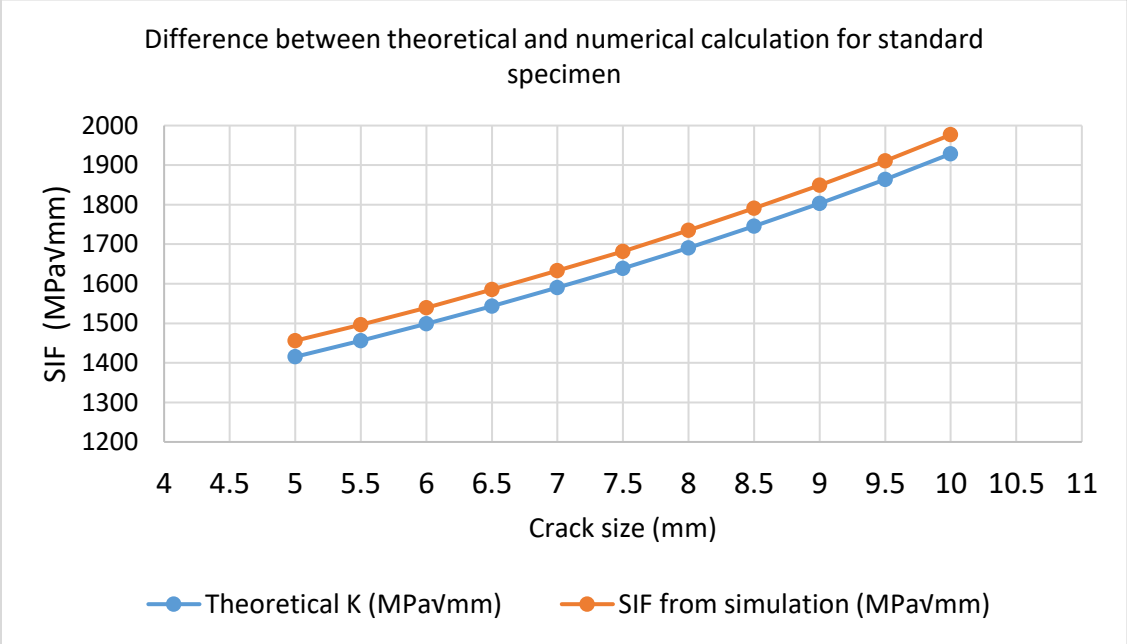

Figure 6.2: Difference between theoretical and numerical calculation for standard specimen

6.2) Results of new specimen

As with the standard specimen, Figure 6.3 shows the SIF distribution through the thickness for the new specimen at a/w = 0.45. Contours 2 through 6 again overlap again completely due to their close numerical agreement, leaving only Contour 1 which departs visibly owing to its proximity to the crack-tip singularity distinguishable in the plot.

Table 6.2 represents the SIFs from the simulation for the new specimen for all crack sizes.

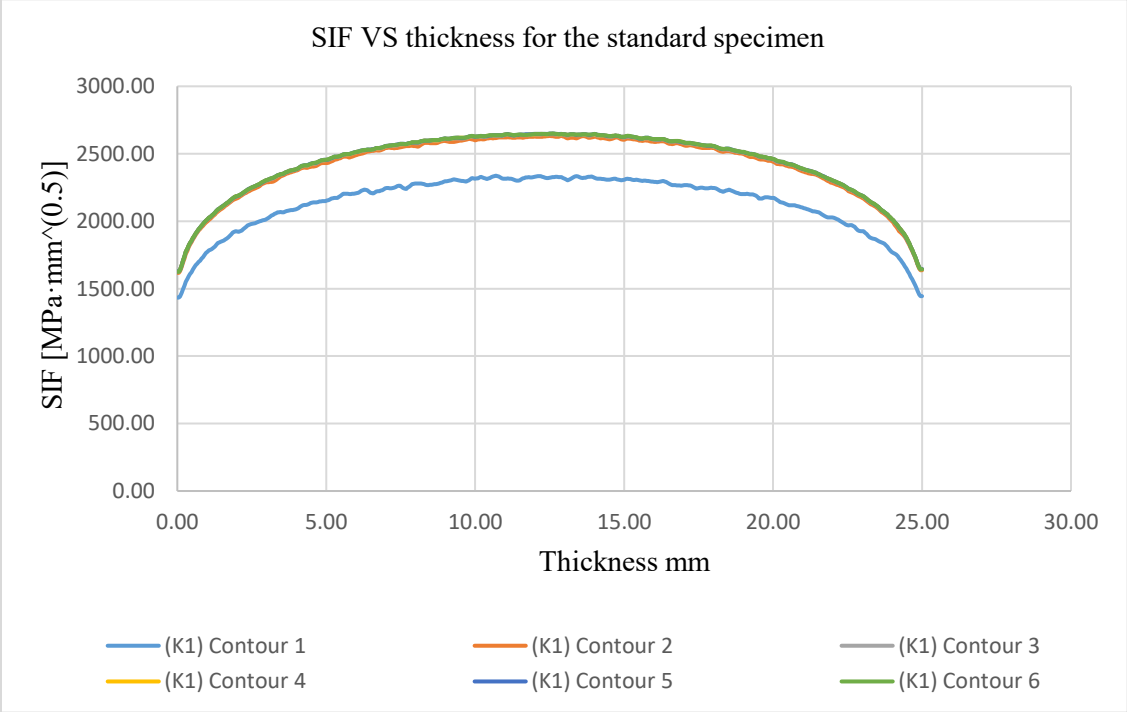

Figure 6.3: the SIF for new specimen for crack size a/w = 0.45

Table 6.2: SIF from the simulation for the new specimen for $(0.45 \leq a/W \leq 0.55)$

crack length (mm)	a/w	K_I for new specimen (MPa√mm)
5.00	0.45	2426.63
5.50	0.46	2466.19
6.00	0.47	2507.89
6.50	0.48	2546.63
7.00	0.49	2589.29
7.50	0.50	2629.49
8.00	0.51	2678.77
8.50	0.52	2722.34
9.00	0.53	2769.75
9.50	0.54	2817.90
10.00	0.55	2868.44

6.3) calibration form from the two specimens

To mathematically characterize the structural behavior of the new specimen and facilitate its future use in physical laboratory testing, customized geometric calibration functions, F(a/W), were derived for both the standard and optimized geometries. In accordance with the fundamental principles of Linear Elastic Fracture Mechanics standardized in ISO 12135, the Mode I Stress Intensity Factor (K_I) is governed by the universal analytical relationship:

$$K_I = \frac{F}{B\sqrt{W}} F\left(\frac{a}{W}\right) \quad \text{Eq.(6.1)}$$

By algebraically inverting this governing law, the dimensionless shape factor can be directly isolated as a function of the numerical outputs:

$$F\left(\frac{a}{W}\right) = \frac{K_I\, B\sqrt{W}}{F} \quad \text{Eq.(6.2)}$$

Plotting $\frac{K_I\, B\sqrt{W}}{F}$ against the corresponding a/W ratio allows then to induce a relationship between $F\left(\frac{a}{W}\right)$ and $\left(\frac{a}{W}\right)$ for both the standard and the new specimen.

A polynomial curve was then fitted to this data set, yielding an empirical calibration formula that expresses calibration formula as a function of a/W

Table 6.3 summarizes the results obtained for both the standard and new specimen geometries across the investigated range of crack lengths. For standard specimen, the theoretical and simulated Mode I stress intensity factors are reported, along with the corresponding normalized geometric factor $F\left(\frac{a}{W}\right) = \frac{K_I\, B\sqrt{W}}{F}$, calculated using the simulated K values. And, for new specimen, simulated Mode I stress intensity factors are also reported, along with the corresponding geometric factor $F\left(\frac{a}{W}\right) = \frac{K_I\, B\sqrt{W}}{F}$.

Table 6.3: Comparison of theoretical and numerical calculation for Stress Intensity Factors for standard and new specimens

Crack length (mm)	a/W	Theoretical K (MPa√mm) for Standard specimen	K_I From simulation (MPa√mm) Standard specimen	K_I from simulation (MPa√mm) New specimen	Formula (KB(W^0.5))/F for Standard specimen	Formula (KB(W^0.5))/F for new specimen
5	0.45	1415.27	1455.97	2426.63	8.58	14.30
5.5	0.46	1455.98	1496.60	2466.19	8.82	14.53
6	0.47	1498.57	1539.63	2507.89	9.07	14.78
6.5	0.48	1543.19	1585.59	2546.63	9.34	15.01
7	0.49	1590.00	1632.98	2589.29	9.62	15.26
7.5	0.50	1639.20	1682.06	2629.49	9.91	15.49
8	0.51	1690.98	1734.86	2678.77	10.22	15.78
8.5	0.52	1745.56	1790.93	2722.34	10.55	16.04
9	0.53	1803.17	1849.58	2769.75	10.90	16.32
9.5	0.54	1864.08	1911.04	2817.90	11.26	16.60
10	0.55	1928.58	1976.73	2868.44	11.65	16.90

Figure 6.4 presents the calibration formula for both the standard and new low-volume specimens, over the ASTM E1820 range $0.45 \leq a/W \leq 0.55$. Both datasets are fitted with third-order polynomials, yielding near-unity coefficients of determination ($R^2 = 1$ for the standard specimen, $R^2 = 0.9999$ for the new specimen), confirming excellent agreement between the fitted curves and the simulated data.

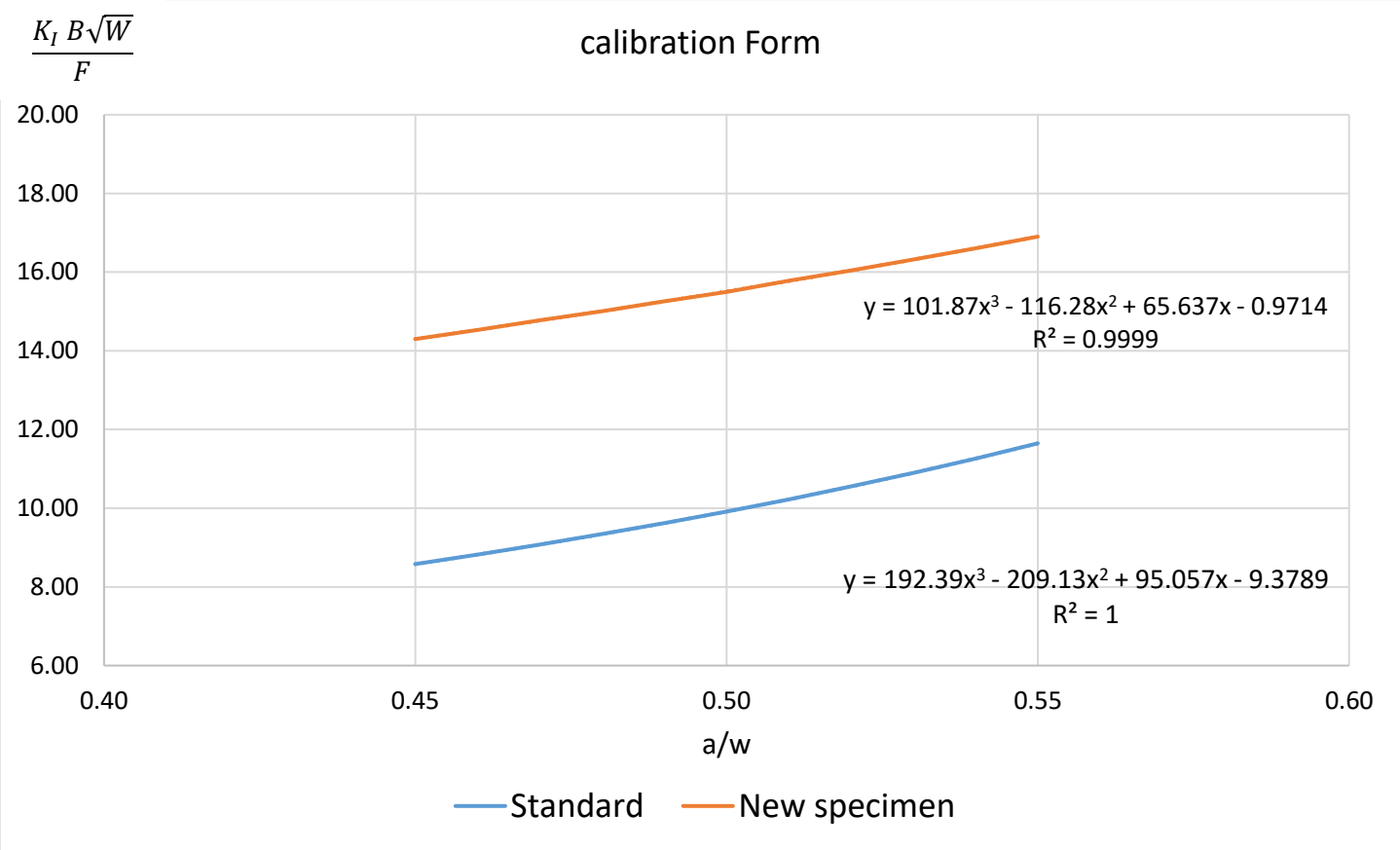

Figure 6.4: the calibration forms for both the standard and the new specimen

So, the calibration form for the standard specimen is

$y = 192.39x^3 - 209.13x^2 + 95.057x - 9.3789$ Eq.(6.3)

and where $y = \frac{K B\sqrt{W}}{F} = F\left(\frac{a}{w}\right)$ and $x = \frac{a}{w}$

So we will have

$$\boldsymbol{F\left(\frac{a}{W}\right) = 192.39\left(\frac{a}{w}\right)^3 - 209.13\left(\frac{a}{w}\right)^2 + 95.057\left(\frac{a}{w}\right) - 9.3789}$$ Eq.(6.4)

and the calibration form for the New specimen is

$y = 101.87\ x^3 - 116.28\ x^2 + 65.637\ x - 0.9714$ Eq.(6.5)

and where $y = \frac{K B\sqrt{W}}{F} = F\left(\frac{a}{W}\right)$ and $x = \frac{a}{w}$

So we will have

$$\boldsymbol{F\left(\frac{a}{W}\right) = 101.87\left(\frac{a}{W}\right)^3 - 116.28\left(\frac{a}{W}\right)^2 + 65.637\left(\frac{a}{W}\right) - 0.9714}$$ Eq.(6.6)

In order to make the stress intensity factor values for the standard specimen from the numerical simulation exactly equal to the theoretical ASTM formula, an empirical correction factor of 0.975 was introduced. This factor was derived from the average percentage discrepancy (approximately 2.6%) observed between the simulated and theoretical K values across the investigated range of crack lengths. By multiplying calibration formulas with this correction factor, the resulting values align with the ASTM theoretical formula, thereby validating the numerical model and providing a refined calibration reference for subsequent plastic model.

So, the final calibration formula for the standard specimen will be

$$\boldsymbol{F\left(\frac{a}{W}\right) = 0.975 \times (192.39\left(\frac{a}{w}\right)^3 - 209.13\left(\frac{a}{w}\right)^2 + 95.057\left(\frac{a}{w}\right) - 9.3789)}$$ Eq.(6.7)

And for new specimen

$$\boldsymbol{F\left(\frac{a}{W}\right) = 0.975 \times (101.87\left(\frac{a}{W}\right)^3 - 116.28\left(\frac{a}{W}\right)^2 + 65.637\left(\frac{a}{W}\right) - 0.9714)}$$ Eq.(6.8)

Chapter 7: plastic Fracture Model for the standard specimen

The fundamental objective of conducting the non-linear plasticity simulation is to comparatively analyze the localized plastic deformation specifically, the size and geometric evolution of the plastic zone between a standard fracture mechanics specimen and a low-volume specimen. To ensure methodological validity, this comparative analysis must be evaluated under equivalent fracture conditions, meaning both models are subjected to the same Mode I stress intensity factor (K_I).

The verification of the low-volume design is strongly dependent on the correlation of the morphological characteristics of its respective plastic zone with that of the standard geometry.

The design changes and the computational model can be validated if the simulation demonstrates that the low-volume specimen plastic zone closely resembles the standard specimen similar in size and geometric shape. On the contrary, if the low-volume specimen displays a considerably larger plastic zone or irregularity in this compare to the standard model, it shows a loss of mechanical constraint. In such circumstances, it requires geometric recalibration by mainly altering the width (W) and thickness (B) of the smaller specimen, which would cancel the advantage of reduced volume. Mainly done to ensure it better contains the yielding region and maintains plane strain conditions.

The von Mises yield criterion was applied to determine the onset of plastic deformation under multi-axial stress states, which is mathematically expressed in terms of principal stresses as:

$$\sigma_e = \frac{1}{\sqrt{2}}\sqrt{(\sigma_1 - \sigma_2)^2 + (\sigma_2 - \sigma_3)^2 + (\sigma_1 - \sigma_3)^2} = \sigma_y \qquad \text{Eq.(7.1)}$$

Where σ_e represents the equivalent von Mises stress, and σ_1 , σ_2, σ_3 are the principal stresses

The elastic-plastic finite element model was developed to calculate and visualise the plastic zone that forms ahead of the crack tip as the applied load increases. Rather than assuming small-scale yielding as in the elastic analysis, this model allows the material to yield progressively, tracking how the plastic region grows and changes shape as the load is ramped from zero to its full value.

The loading was applied as a force-controlled ramp, which means the solver increases the load incrementally and at each step checks whether the material has yielded and by how much. This approach captures the full transition from elastic behaviour — where the stress intensity factor alone describes the crack-tip field — into the regime where a significant plastic zone has developed and the distribution of equivalent plastic strain must be examined directly.

Once the solution is complete, the equivalent plastic strain contours are extracted from the results. These contours will show exactly where yielding has occurred, how far the plastic zone extends from the crack tip, and what shape it takes through the specimen thickness. This information is then used to compare the standard CT specimen against the proposed low-volume geometry, ensuring that both specimens are evaluated at the same K_I levels and that any differences in plastic zone size or shape are attributed to geometry alone rather than differences in loading or material response.

7.1) Plastic Material characteristics

The elastic-plastic finite element model was assigned a constitutive material, comprising two coupled components: a linear elastic response and a rate-independent plastic hardening law.

The elastic response was defined through isotropic elasticity, with a Young's modulus of **200 GPa** and a Poisson's ratio of **0.3**. These values are consistent with those used in the preceding elastic analysis, ensuring continuity between the two modelling phases.

The plastic response was defined using a **Bilinear Isotropic Hardening (BISO)** model, which characterises the post-yield behaviour of the material through two parameters: a yield strength of **800 MPa** and a plastic tangent modulus of **3019 MPa**. Below the yield threshold, the material response remains entirely elastic and fully reversible. Once the stress at any point in the model reaches 800 MPa, the material yields and plastic strain is added. The isotropic hardening assumption implies that the yield surface expands uniformly in all stress directions as plastic strain accumulates, which is physically appropriate for the monotonic, single-cycle loading applied in this analysis.

It should be noted that the Bilinear model represents a simplification of the actual stress-strain response of the material, which in reality exhibits a more gradual transition through yielding. However, given that the primary objective of the elastic-plastic analysis is to determine the size and spatial extent of the plastic zone rather than to characterise post-fracture deformation in detail, the bilinear idealisation is considered a reasonable and computationally efficient approximation for the purposes of this study.

7.2) Trying with 3d model

While the 3D finite element framework accurately captured the linear elastic fracture response, extending it to non-linear elastoplastic analysis proved computationally impractical. Resolving the localized plastic zone required a highly refined mesh across the full thickness, yielding an exponential rise in nodes (23,221,481) and elements (17,272,255). The resulting system of non-linear equations exceeded the memory and processing capacity of standard non-cluster workstations. This computational bottleneck necessitated transitioning from the full 3D model to computationally efficient 2D bounding model (plane strain), representing the physical extremes of the specimen without the associated hardware limitations.

7.3) building the model

To faithfully replicate the physical testing conditions while drastically reducing the computational overhead associated with the previous 3D model, the macroscopic geometric boundaries were projected onto a 2D planar domain. Crucially, to ensure this 2D simplification remains mechanically valid and accurately represents the most critical region of the physical specimen, the numerical solver was explicitly configured to operate under the assumption of Plane Strain.

Plane strain represents the approximation of the mid-plane condition, corresponding to maximum constraint. For this elastoplastic comparative analysis, a fixed crack length a/w= 0.5 was strategically selected for both the standard and low volume models, providing a critical baseline to accurately evaluate yielding containment and localized mechanical constraint.

In the continuum mechanics of solid bodies, a Plane Strain state describes a condition where the material is assumed to be infinitely thick, or where its out-of-plane boundaries are strictly prevented from displacing.

Mathematically, if the specimen geometry lies in the x-y plane, the plane strain formulation dictates that all normal and shear strains in the transverse thickness direction (z-axis) are identically zero:

$$\epsilon_z = 0 \ , \ \gamma_{xy}=0 \ , \ \gamma_{yz}=0 \qquad \text{Eq.(7.2)}$$

Because the physical material at the core of the specimen is rigidly flanked by the surrounding bulk material, it cannot freely contract inward (the Poisson effect) when the specimen is pulled apart in the y-direction. Since the strain is restricted ($\epsilon_z = 0$), a highly elevated out-of-plane normal stress (σ_z) is subsequently generated.

The presence of the induced (out-of-plane) stress σ_z creates a severe state of triaxial tensile stress immediately ahead of the crack tip. This triaxiality severely inhibits the material's ability to yield and flow plastically. By suppressing plasticity, the plane strain condition minimizes the size of the plastic zone, thereby forcing the material to fail in its most brittle, conservative, and dangerous mode. Therefore, defining this 2D model under plane strain conditions provides the most rigorous, standard-compliant baseline for evaluating whether the new specimen can successfully contain yielding to the same restrictive degree as the bulky standard geometry.

7.4) Coordinate system and symmetry, symmetry and meshing

To create a meshing refinement in the crack front and evaluate the fracture mechanics parameters and appropriately define the crack-tip kinematics, a localized Cartesian coordinate system was explicitly established at the crack front. For this specific elastoplastic analysis, the origin of this local coordinate system was positioned precisely at the crack tip figure 7.1, corresponding to the selected absolute crack length. In accordance with standard theoretical fracture mechanics conventions, the local X-axis was aligned parallel to the anticipated direction of crack propagation. Also, in order to reduce computational demand, geometric and loading symmetry were exploited. Since both specimens and their Mode I loading are symmetric about the vertical axis, only half the 2D geometry was modelled. A frictionless support (symmetry) condition was applied along the uncracked ligament, constraining normal displacement (Ux = 0) while permitting lateral deformation. This halved nodes and degrees of freedom, accelerating solution.

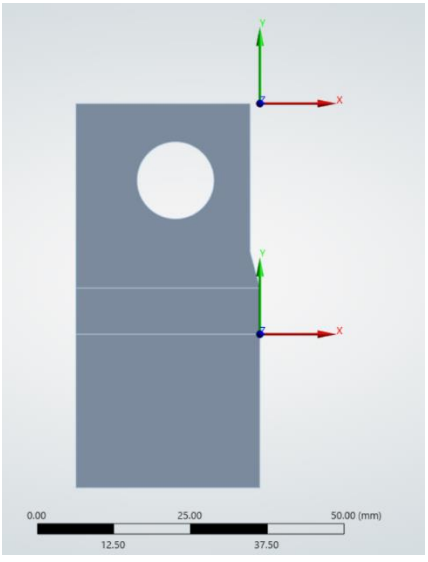

Figure 7.1: local coordinate system

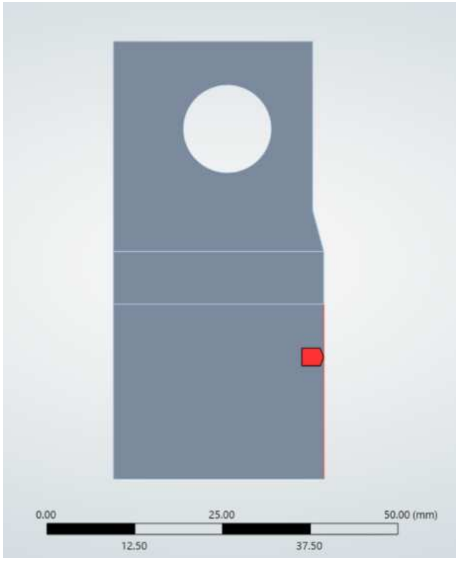

Figure 7.2: symmetry condition

In the 2D plane strain model, a three-zone meshing strategy was adopted: a coarse mesh in regions distant from the crack tip, and a highly refined mesh at the crack tip, within the local coordinate system, using a sphere of influence of radius 2 mm and element size 0.02 mm. To ensure a smooth mesh transition, a nested sphere of influence of radius 10 mm and element size 0.5 mm was additionally applied in the same local coordinate system.

The discretized model comprises a total of **71641 nodes** and **35665 elements**. Figure 7.3 represents the meshing of the whole part, Figure 7.4 represent the refinement area, Figure 7.5 represents the gradient from the fined meshed zone to the coarse one.

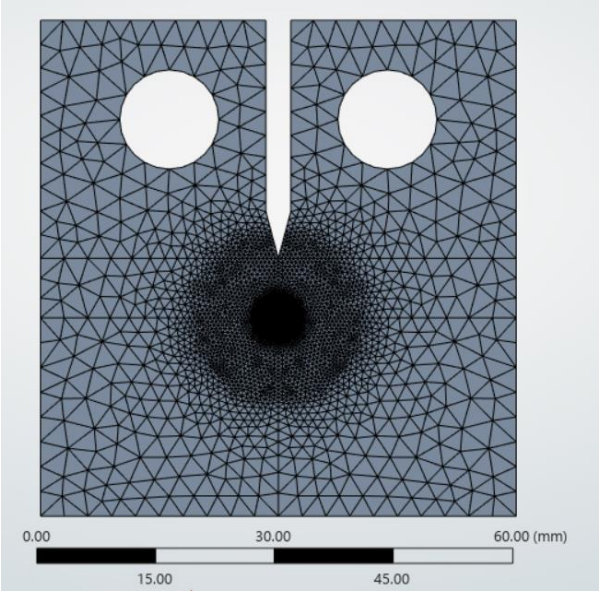

Figure 7.3: meshing of the whole part

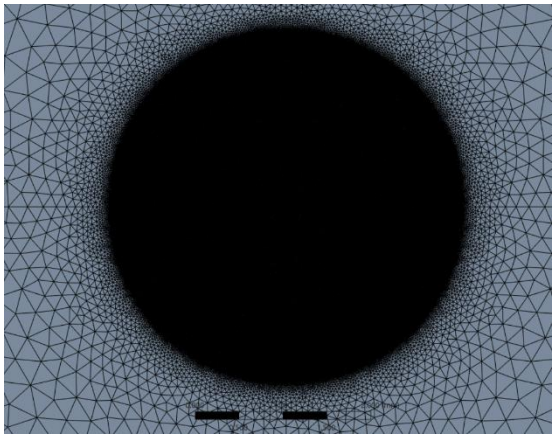

Figure 7.4: the refinement area

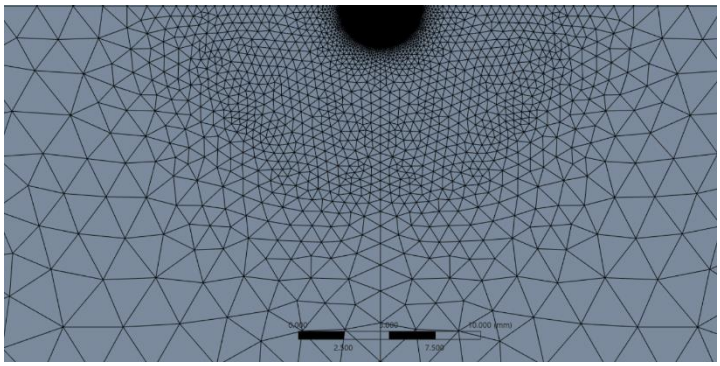

Figure 7.5: the gradient of the meshing

7.5) Boundary condition

To ensure a rigorous and standardized comparative analysis of the elastoplastic behavior, it was imperative to subject the two-dimensional numerical models to an equivalent, critically valid fracture driving force. The applied mechanical load (P) required for the elastoplastic simulations was analytically derived based on the geometric size requirements for valid plane-strain fracture toughness testing.

The baseline Compact Tension (CT) specimen is defined by the following constant geometric and material parameters: an effective width of W = 50 mm, a standard thickness of B = 25 mm, an absolute crack length of a = 25 mm, yielding a normalized ratio of a/W = 0.5), and an material yield strength of 800 MPa.

According to standard fracture mechanics validity criteria, the maximum measurable Mode I Stress Intensity Factor (KI) before the loss of high geometric constraint is governed by the uncracked ligament size limit:

$$W\text{-}a = 2.5\left(\frac{KI}{\sigma}\right)^2 \qquad \text{Eq.(7.3)}$$

By rearranging this inequality to evaluate the bounding limit case, the maximum valid driving force capable of being sustained by the specimen can be established:

$$KI = \sigma * \sqrt{\frac{W-a}{2.5}} \qquad \text{Eq.(7.4)}$$

Substituting the physical parameters of the specimen yields:

$$KI = 800 * \sqrt{\frac{50-25}{2.5}} = 80\ \text{MPa}\sqrt{m} \qquad \text{Eq.(7.5)}$$

The applied load required to generate this critical crack-tip condition is computed by utilizing the standard linear elastic calibration function:

$$P = \frac{K\ B\ \sqrt{W}}{F\left(\frac{a}{W}\right)} \qquad \text{Eq.(7.6)}$$

For standard specimen, the geometry shape will be used is :

$$\boldsymbol{F\left(\frac{a}{W}\right) = 0.975 \times \left(192.39\left(\frac{a}{W}\right)^3 - 209.13\left(\frac{a}{W}\right)^2 + 95.057\left(\frac{a}{W}\right) - 9.3789\right)}$$

$$\boldsymbol{F\left(\frac{a}{W}\right) = 0.975 \times \left(192.39\left(\frac{25}{50}\right)^3 - 209.13\left(\frac{25}{50}\right)^2 + 95.057\left(\frac{25}{50}\right) - 9.3789\right) = 9.667}$$

So the applied force $= \frac{K\ B\ \sqrt{W}}{F\left(\frac{a}{W}\right)} = = \frac{80\ \text{MPa}\sqrt{m} * 25\ mm * \sqrt{50}\ \sqrt{mm}}{9.6671}$

The units work out to force (Newton), since MPa = N/m².

Converting everything to meters first: B = 0.025 m, $\sqrt{W} = \sqrt{0.05}$ m = 0.2236 $\sqrt{m}$ and Numerator = 80 MPa·$\sqrt{m}$× 0.025 m × 0.2236 $\sqrt{m}$ = 0.4472 MPa·m²

So, Force = 0.4472 / 9.667= 0.046260 MPa·m² and Since 1 MPa·m² = 10^6 N: So, **Force = 46260 N**

Within the ANSYS numerical environment, two-dimensional plane strain elements are mathematically formulated based on an assumed uniform out-of-plane unit thickness (typically 1mm). Consequently, the total macroscopic boundary force calculated for the full three dimensional specimen cannot be applied directly to the 2D planar model. To preserve absolute mechanical equivalence between the physical reality and the two-dimensional simulation, the total global load must be normalized by the specimen's actual physical thickness (B = 25mm). This transformation converts the total absolute force into an equivalent distributed line load, expressed as force per unit thickness. Therefore, utilizing the target total boundary load (**46260** N), the actual load prescribed at the theoretical pin nodes of the plane strain model is calculated by dividing this total force by the 25 mm thickness. This yields an adjusted, dimensionally consistent driving force of 1850 N/mm, ensuring the 2D crack tip experiences the exact same mechanical driving energy as the mid-plane of the physical 3D specimen.

The single continuous constraint applied to the bottom edge (the uncracked ligament ahead of the crack tip). This single boundary condition effectively replaces the structural stiffness and kinematic resistance of the omitted lower half of the specimen. Figure 7.6

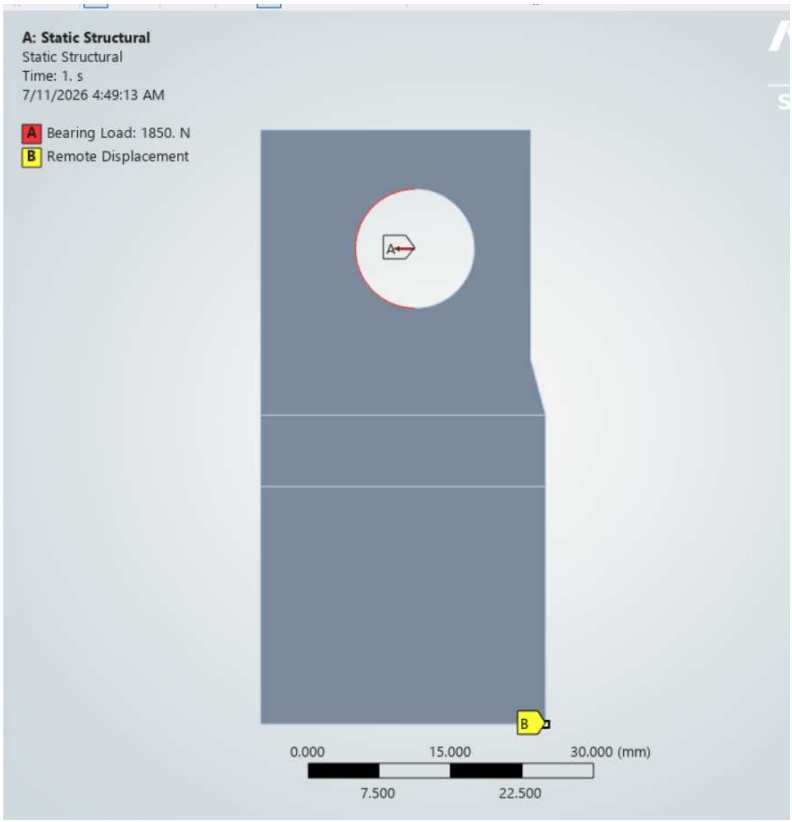

Figure 7.6: Boundary condition

Chapter 8 : plastic Fracture Model for the new specimen

8.1) New specimen building

For the new low-volume specimen, the same material characteristics, coordinate system Figure 8.1, symmetry conditions Figure 8.2, and meshing strategy applied to the standard specimen were adopted, ensuring methodological consistency between the two models. Figure 8.3, 8.4

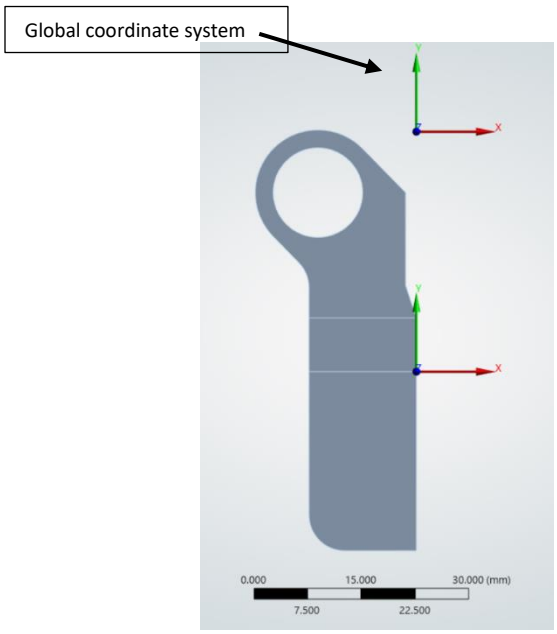

Figure 8.1: coordinate system

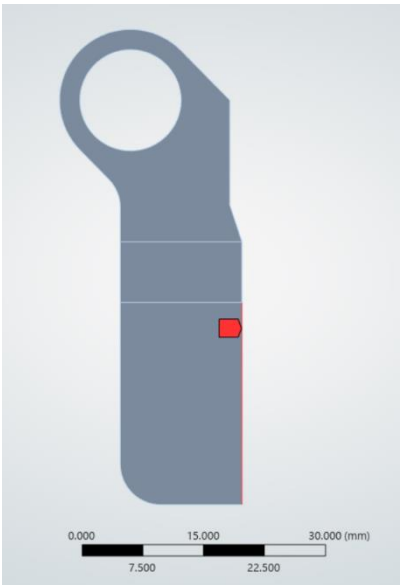

Figure 8.2: symmetry condition

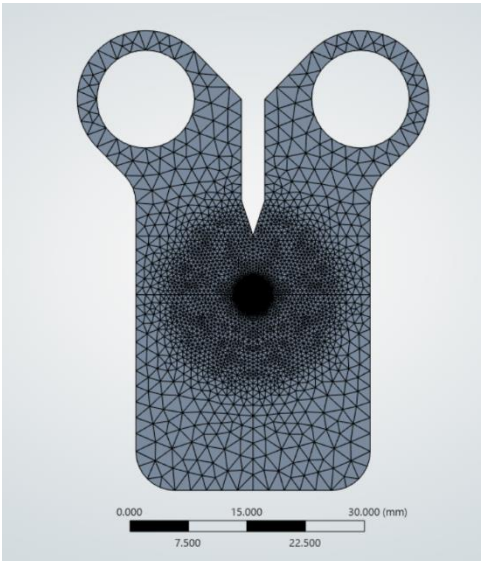

Figure 8.3: the part meshing

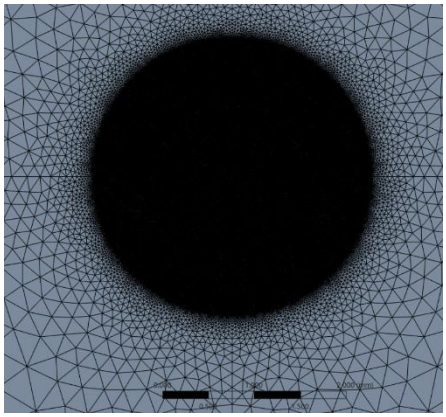

Figure 8.4: the refinement zone

8.2) Boundary condition

The applied mechanical load (P) used in the elastoplastic simulations was therefore derived analytically, based on the geometric size requirements for a valid plane-strain fracture toughness test. As mentioned in the previous chapter, the theoretical Mode I Stress Intensity Factor (KI) is the same for standard and new specimens according to equations 8.1, 8.2

$$W\text{-}a = 2.5 \times \left(\frac{K_I}{\sigma}\right)^2 \quad \text{Eq.(8.1)}$$

By rearranging this inequality to evaluate the bounding limit case, the maximum valid driving force capable of being sustained by the specimen can be established:

$$K_I = \sigma * \sqrt{\frac{W-a}{2.5}} \quad \text{Eq.(8.2)}$$

Substituting the physical parameters of the specimen yields:

$$K_I = 800 * \sqrt{\frac{50-25}{2.5}} = 80 \text{ MPa}\sqrt{m} \quad \text{Eq.(8.3)}$$

The applied load required to generate this critical crack-tip condition is computed by utilizing the standard linear elastic calibration function:

$$P = \frac{K_I B \sqrt{W}}{F\left(\frac{a}{W}\right)} \quad \text{Eq.(8.4)}$$

For the new specimen. the geometry shape will be used is :

$$\boldsymbol{F\left(\frac{a}{W}\right) = 0.975 \times \left(101.87 \left(\frac{a}{W}\right)^3 - 116.28 \left(\frac{a}{W}\right)^2 + 65.637 \left(\frac{a}{W}\right) - 0.9714\right)}$$

$$\boldsymbol{F\left(\frac{a}{W}\right) = 0.975 \times \left(101.87 \left(\frac{25}{50}\right)^3 - 116.28 \left(\frac{25}{50}\right)^2 + 65.637 \left(\frac{25}{50}\right) - 0.9714\right) = 15.123}$$

So the applied force $= \frac{K_I B \sqrt{W}}{F\left(\frac{a}{W}\right)} = = \frac{80 \text{ MPa}\sqrt{m} * 25\ mm * \sqrt{50}\sqrt{mm}}{15.123}$

Converting everything to meters first: B = 0.025 m. $\sqrt{W} = \sqrt{0.05}$ m = 0.2236 $\sqrt{m}$ and Numerator = 80 MPa·$\sqrt{m}$× 0.025 m × 0.2236 $\sqrt{m}$ = 0.4472 MPa·m²

So. Force = 0.4472 / 15.123 = 0.029570 MPa·m² and Since 1 MPa·m² = 10^6 N:

Force = 29570 **N**

Within the ANSYS numerical environment, two-dimensional plane strain elements are mathematically formulated based on an assumed uniform out-of-plane unit thickness (typically 1mm). Consequently, the total

macroscopic boundary force calculated for the full three dimensional specimen cannot be applied directly to the 2D planar model. To preserve absolute mechanical equivalence between the physical reality and the two-dimensional simulation, the total global load must be normalized by the specimen's actual physical thickness (B = 25mm). This transformation converts the total absolute force into an equivalent distributed line load, expressed as force per unit thickness. Therefore, utilizing the target total boundary load (28833 N), the actual load prescribed at the theoretical pin nodes of the plane strain model is calculated by dividing this total force by the 25 mm thickness. This yields an adjusted, dimensionally consistent driving force of 1182 N/mm, ensuring the 2D crack tip experiences the exact same mechanical driving energy as the mid-plane of the physical 3D specimen.

A single continuous boundary condition was applied along the bottom edge, corresponding to the uncracked ligament ahead of the crack tip. This constraint effectively prevent the specimen from moving in the space with no limitation. Figure 8.5

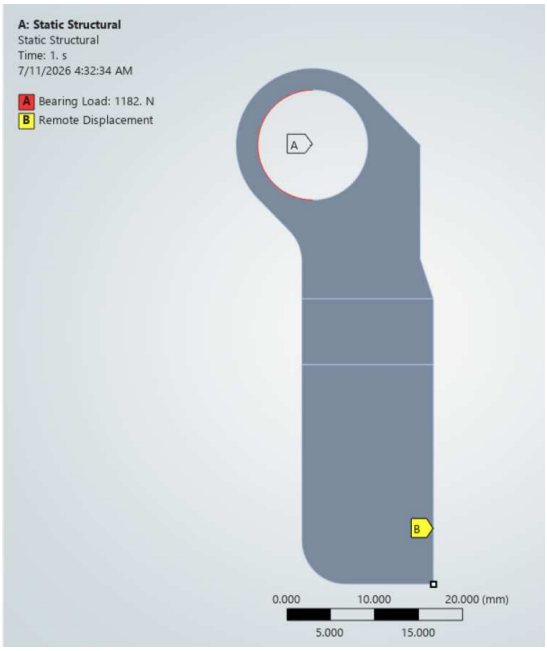

Figure 8.5: boundary condition

Chapter 9 : Results of plastic model for standard specimen and new specimen

Following the execution of the non-linear elastoplastic simulations, the primary metric for comparison between the standard and low-volume specimens will be the physical size, shape, and containment of the crack-tip plastic zone. In fracture mechanics testing, the extent of this localized yielding is the critical factor that dictates the preservation of Small-Scale Yielding conditions, which is strictly required for valid K_I evaluations. If the numerical results demonstrate that the low-volume specimen restricts the plastic zone to a nearly identical geometric envelope as the standard geometry under equivalent driving forces, it conclusively proves that the new design maintains the necessary macroscopic mechanical constraint. Consequently, demonstrating this plastic equivalence will mathematically and mechanically justify substituting the traditional, bulky specimen with the lightweight variant in physical laboratory testing successfully reducing additive manufacturing material consumption and print times without compromising the standardized validity of the fracture toughness results.

As mentioned before, The standard specimen has a volume of 85483 mm^3 and a mass of 0.666 kg, while the low-volume specimen reduces this to 39184 mm^3 and 0.307 kg. Replacing the standard geometry with the low-volume one therefore yields a 53% reduction in material consumption.

9.1) plastic zone

The comparison between the standard and new specimens was restricted to plane strain model, since plane strain represents the more conservative and physically representative condition at the crack tip for specimens of this thickness (B = 25 mm). Under plane strain, the through-thickness constraint suppresses out-of-plane deformation, leading to a tri-axial stress state that more accurately captures the stress intensification and limited plastic zone size typical of thick fracture specimens, consistent with ASTM E399 requirements for valid fracture toughness testing. So, plane strain ensures that the evaluation of the new specimen's plastic zone and stress distribution remains consistent with the fracture mechanics assumptions governing the standard specimen.

To enable a consistent comparison between the two specimen geometries, the same stress legend was applied to both Equivalent (von-Mises) Stress plots for plane strain models, with the lower bound fixed at 800 MPa, corresponding to the material's yield strength. This isolates and highlights the plastic zone in each case, making it possible to directly visualize the extent of yielded material around the crack tip for both the standard and new configurations. Additionally, both results were displayed at true scale (1.0) Figures 9.1, 9.2 , ensuring that the relative size and geometry of the plastic zones can be compared without distortion introduced by deformation scaling. Figures 9.3, 9.4 indicate the plastic zone area for both specimen.

Figure 9.1: Equivalent (von-Mises) Stress for the standard specimen

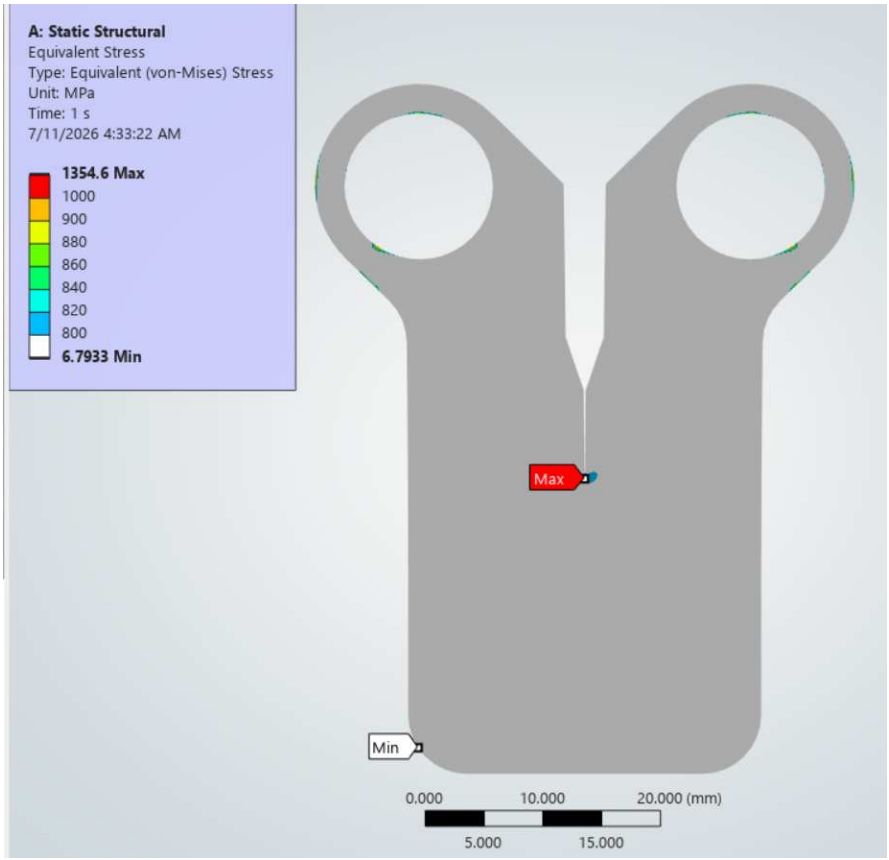

Figure 9.2: Equivalent (von-Mises) Stress for the new specimen

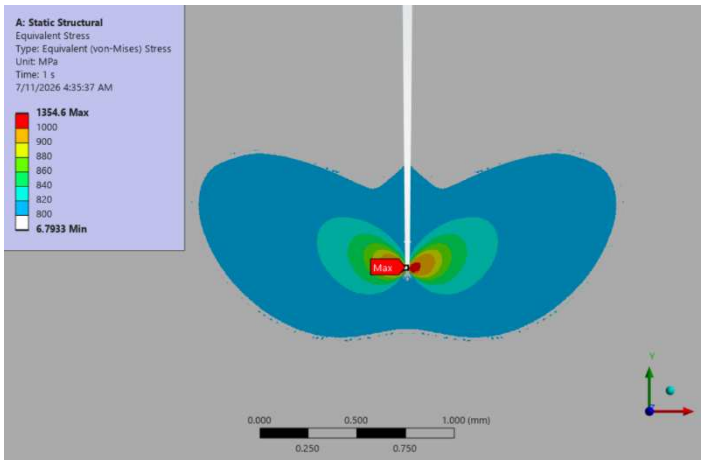

Figure 9.3: plastic zone for the new specimen

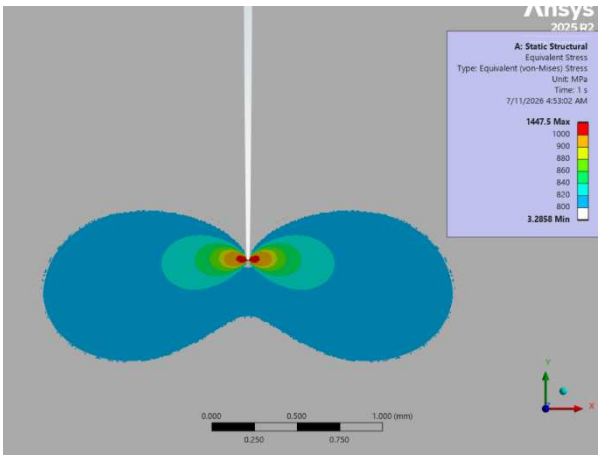

Figure 9.4: plastic zone for the standard specimen

The figure (9.5) presents a comparison of plastic zone area between the standard and new specimens under plane strain conditions, shown both as a bar chart. The standard specimen exhibits a plastic zone area of 1.720 mm², while the new specimen shows a closer value of 1.701 mm², with a difference between them of 2.09 %.

This difference indicates that despite the significant reduction in overall specimen volume, the crack-tip plastic zone size remains nearly unchanged between the two geometries. This is the key justification for adopting the new specimen: the process was deliberately constrained by an exclusion region sized using plastic zone area. As a result, the fracture critical zone, where plastic deformation govern the validity of fracture toughness measurements, is preserved almost identically to the standard specimen. Since the plastic zone size is a key parameter, the close agreement between the two specimens demonstrates that the new geometry maintains the same fracture mechanics behavior as the standard one. This means the new specimen can reliably replace the standard specimen in testing, offering substantial material and cost savings without compromising the accuracy or validity of the fracture toughness results.

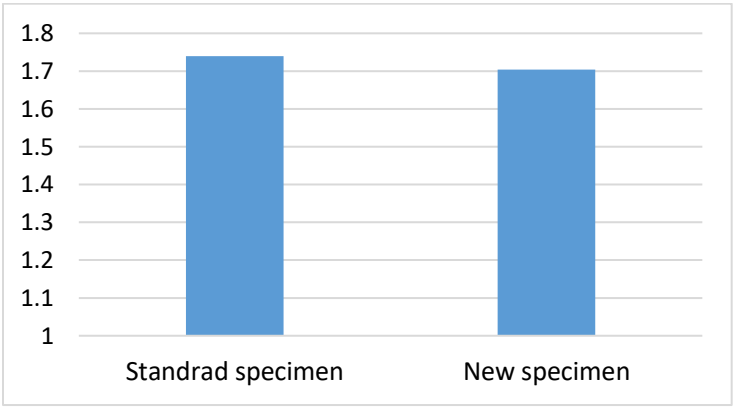

Figure 9.5: the comparison between plastic zone areas

9.2) uncracked ligament stress

To assess the load-bearing behavior of the remaining material, the σ_{xx} was measured along a defined path through the uncracked ligament for both the standard and new specimens Figures 9.6, 9.7, extending from the crack tip toward the back face. The resulting stress along x axis distributions Figure 9.8 are nearly identical between the two geometries throughout the ligament, indicating that the new specimen sustains essentially the same internal stress state as the standard one despite its significantly reduced mass. This agreement is a strong indicator of mechanical equivalence: the process successfully removed material from non-critical regions without altering the load transfer path through the uncracked ligament from 1 to 2 in the, meaning the new specimen achieves comparable structural performance and stress-carrying capacity while using substantially less material.

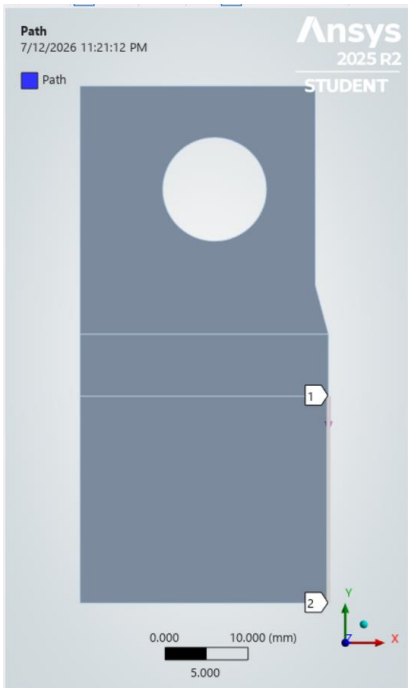

Figure 9.6: path of un-cracked ligament in the standard specimen from 1 to 2

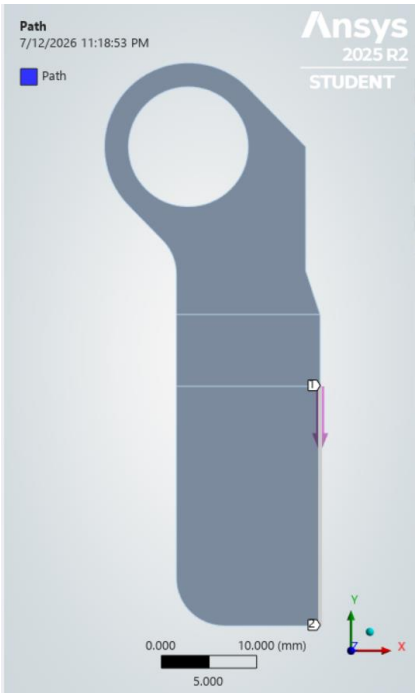

Figure 9.7: path of uncracked ligament in the new specimen from 1 to 2

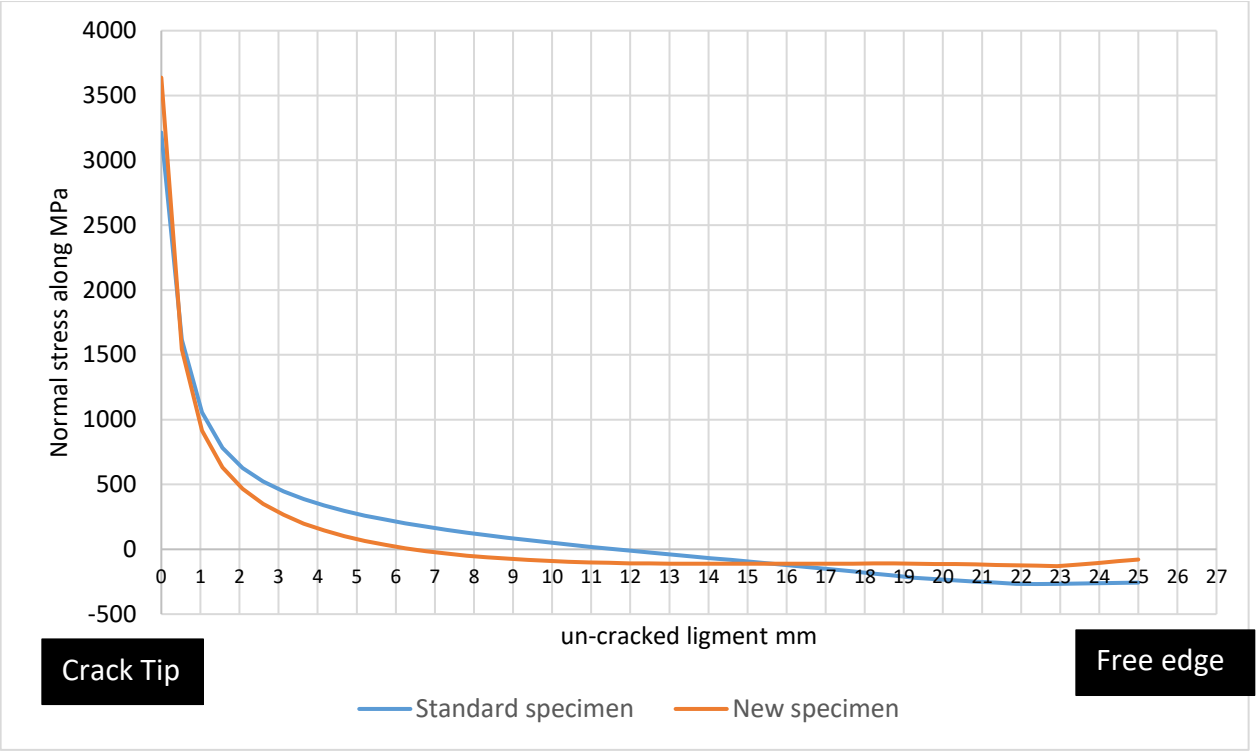

Figure 9.8: the comparison between the stress along un-cracked ligament

For more detailed analysis of the near-tip stress fields, the normal stress distribution along the uncracked ligament was replotted using a logarithmic (log-log) scale. This representation isolates the critical region immediately ahead of the crack tip, allowing for a direct comparison between the simulated specimen geometries and the theoretical linear elastic fracture mechanics solution ($\sigma = K_I / \sqrt{2\pi r}$). As shown in the log-log plot figure (9.9), the simulated stresses exhibit a linear trend in the immediate vicinity of the crack tip that closely aligns with the theoretical elastic formulation. Furthermore, as the distance from the crack tip increases, the normal stress in the physical specimens transitions from tensile to compressive to maintain internal force equilibrium. Because logarithmic scales cannot accommodate negative values, the simulated curves naturally drop off and terminate at the exact coordinates where the stresses cross the zero axis.

As distinctly observed in the logarithmic plot, the normal stress distributions for both the standard and new specimens converge and perfectly overlap with the theoretical elastic formulation in the region immediately adjacent to the crack tip. This initial alignment is theoretically expected; within this highly localized area, the stress field is strictly governed by the stress intensity factor (K_I) and mathematically follows the $\frac{1}{\sqrt{r}}$ singularity, characteristic of the K-dominated region. This near-tip overlap provides critical evidence that the newly proposed low-volume geometry successfully reproduces the identical singular stress field as the standard CT specimen, prior to the expected divergence caused by finite boundary effects.

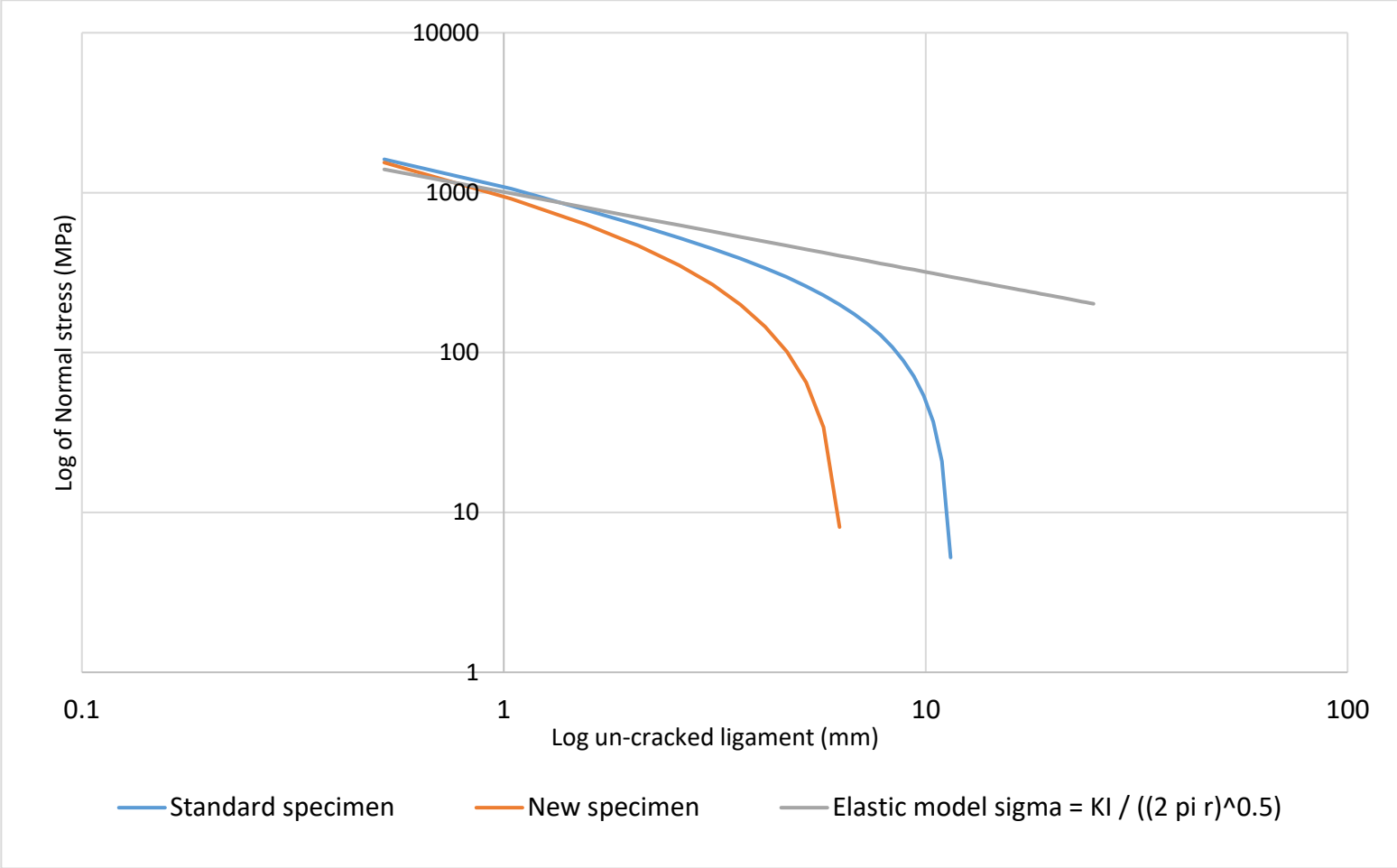

Figure 9.9: Log-log plot of normal stress along the un-cracked ligament.

Conclusion

This thesis introduced a low-volume specimen designed to characterize Mode I plane-strain fracture toughness in additively manufactured metallic alloys, while substantially reducing material consumption and build time.

The specimen volume was reduced from 85483 mm³ to 39184 mm³, achieving a 53% reduction in material consumption while preserving the same thickness (B) and uncracked ligament width (W) required for plane-strain validity.

Linear elastic FEM simulations were used to derive calibration formulas relating applied load, crack length, and the Mode I stress intensity factor, providing the analytical foundation needed to compute fracture-driving loads for the new geometry.

Elastoplastic analyses comparing the standard and new specimens under plane strain conditions for the same K_I showed close agreement in crack-tip plastic zone areas: 1.720 mm² for the standard specimen and 1.701 mm² for the new specimen, a difference of 2.09 %, confirming that small-scale yielding conditions are nearly the same in the new design.

Stress distributions along the uncracked ligament, including both the normal force and σ_{xx} along the crack plane, were nearly identical between the two specimens, indicating that the new geometry sustains an equivalent internal stress state despite its reduced mass.

These results demonstrate that the low-volume specimen reproduces the fracture-governing mechanics of the standard CT geometry with high fidelity. The close agreement in plastic zone size and stress fields supports the conclusion that the low-volume design does not compromise the validity of fracture toughness characterization under ASTM E399 and E1820 assumptions.

From a practical standpoint, the substantial reduction in material usage translates directly into lower powder consumption and reduced machine build time for additively manufactured specimens, addressing a key economic barrier to fracture testing of AM components. The proposed geometry therefore offers a numerically validated, cost-effective alternative to conventional CT specimens for AM research and quality control applications.

Future work should focus on physical fabrication and experimental testing of the new specimen to empirically validate the derived calibration functions and confirm the numerically predicted fracture equivalence. Overall, this work establishes a viable pathway toward more efficient and economical fracture toughness testing methodologies for the growing field of additive manufacturing.

Reference

1. Gibson, I., Rosen, D., Stucker, B. (2010). Additive Manufacturing Technologies: 3D Printing, Rapid Prototyping, and Direct Digital Manufacturing. Springer.
2. ASTM E1820: Standard Test Method for Measurement of Fracture Toughness. West Conshohocken, PA: ASTM International.
3. ISO 12135: Metallic materials — Unified method of test for the determination of quasistatic fracture toughness. Geneva, Switzerland: ISO.
4. Ansys Mechanical APDL Fracture Analysis Guide ANSYS, Inc. Release 2025 R1, Southpointe January 2025.
5. Yang, Z. (2025). Application of Finite Element Analysis for Fracture and Damage Mechanics (1st ed.). Boca Raton, FL: CRC Press.
6. Stolarski, T., Nakasone, Yoshimoto, S. (2018). Engineering Analysis with ANSYS Software (2nd ed.). Oxford: Butterworth-Heinemann.
7. T. L. Anderson, Fracture Mechanics: Fundamentals and Applications, 4th ed. Boca Raton, FL: CRC Press, 2017.
8. Minz, S. (2016). 3-D Modelling & Application of Elemental Parabolic Crack Block – ANSYS: An Innovative Approach to Fracture Mechanics Using ANSYS APDL (ANSYS Parametric Design Language). Saarbrücken: LAP LAMBERT Academic Publishing.
9. ANSYS, Inc., ANSYS Mechanical Tutorials, Release 2025 R1. Canonsburg, PA, USA: ANSYS, Inc., 2025
10. Mohammadi, S. (2008). Extended Finite Element Method for Fracture Analysis of Structures. Oxford: Wiley-Blackwell.